



CENTER FOR
MACHINE PERCEPTION



CZECH TECHNICAL
UNIVERSITY

MASTER THESIS

ISSN 1213-2365

Detection of Pulmonary Nodules from CT Scans

Martin Dolejší

dolejm1@fel.cvut.cz

CTU-CMP-2007-05

January 19, 2007

Available at

<http://cmp.felk.cvut.cz/~dolejm1/noduledetection/>

Thesis Advisor: Dr. Ing. Jan Kybic

The CT data were provided by a Faculty Hospital, Motol, Prague.

Program Scan View was provided and supported by RNDr. Jan Krásenský.

This work was supported by the Czech Ministry of Health under project NR8314-3/2005, and by the Grant Agency of the Czech Academy of Sciences under Project 1ET101050403.

Research Reports of CMP, Czech Technical University in Prague, No. 5, 2007

Published by

Center for Machine Perception, Department of Cybernetics
Faculty of Electrical Engineering, Czech Technical University
Technická 2, 166 27 Prague 6, Czech Republic
fax +420 2 2435 7385, phone +420 2 2435 7637, www: <http://cmp.felk.cvut.cz>

Katedra kybernetiky

Školní rok: 2005/2006

ZADÁNÍ DIPLOMOVÉ PRÁCE

Student: Martin Dolejší

Obor: Biomedicínské inženýrství

Název tématu: Detekce plicních modulů

Zásady pro vypracování:

1. Seznamte se s existujícími algoritmy detekce plicních modulů z CT dat.
2. Na jejich základě navrhnete a implementujete vlastní algoritmus.
3. Algoritmus otestujete na dostupných datech.

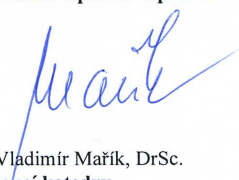
Seznam odborné literatury:

Xiangwei Zhang, Geoffrey McLennan, Eric A. Hoffman, Milan Sonka: Automated Detection of Small-Size Pulmonary Nodules Based on Helical CT Images. IPMI 2005: 664-676

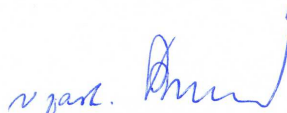
Vedoucí diplomové práce: Dr. Ing. Jan Kybic

Termín zadání diplomové práce: zimní semestr 2005/2006

Termín odevzdání diplomové práce: leden 2007


prof. Ing. Vladimír Mařík, DrSc.
vedoucí katedry




prof. Ing. Vladimír Kučera, DrSc.
děkan

V Praze dne 10.01.2006

Abstract

We present a computer-aided diagnosis (CAD) system to detect small-size (from 2mm to around 10mm) pulmonary nodules from helical CT scans. A pulmonary nodule is a small, round (parenchymal nodule) or worm (juxtapleural nodule) shaped lesion in the lungs. Both have greater radio-density than lungs parenchyma, so they appear white on images. Lung nodules might indicate a lung cancer and their detection in the early stage improves the survival rate of patients. CT is considered to be the most accurate imaging modality for nodule detection. However, the large amount of data per examination makes the interpretation difficult. This leads to omission of nodules by human radiologist. The presented CAD system is designed to help lower the number of omissions and to decrease the time needed to examine the scan by a radiologist. Our system uses two different schemes to locate juxtapleural nodules and parenchymal nodules respectively. For juxtapleural nodules, morphological closing and thresholding is used to find nodule candidates. To locate non-pleural nodule candidates, we use a 3D blob detector based on multiscale filtration. To define which of the nodule candidates are in fact nodules, an additional classification step is applied. Linear and multi-threshold classifiers are used. Ellipsoid model is fitted on nodules to provide geometrical features. System was tested on 18 cases (4853 slices) with total sensitivity of 96%, with about 12 false positives/slice. The classification step reduces the number of false positives to 9 per slice without significantly decreasing sensitivity (89.6%). The algorithm was implemented in Matlab and tested under Windows and Unix system. For easy control simple graphic user interface is included.

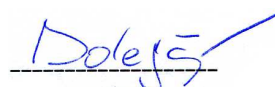
Abstrakt

Tato práce se věnuje vývoji programu pro detekci plicních nodulů. Plicní noduly jsou kulovité nebo červovité útvary v plicích, které jsou na obrázcích z CT zobrazeny světlejšími odstíny oproti plicnímu parenchymu. Detekce plicních nodulů je důležitá, protože se může jednat o rakovinná ložiska, přitom včasná diagnóza zásadně ovlivňuje úspěšnost léčby všech druhů zhoubných onemocnění. Náš CAD (Computer Aided Diagnostic) systém je navržen tak, aby snížil zatížení radiologa při prohlížení velkého množství dat, a zároveň snížil počet přehlédnutých nodulů. Program detekuje odděleně každý ze dvou druhů nodulů. Kulovité (parenchymální) pomocí 3D blobdetektoru (filtrační algoritmus pracující ve více měřítkách) a červovité (juxtapleurální) pomocí prahování a metod matematické morfologie. Ke všem detekovaným objektům přiřadíme elipsoid popisující jejich tvar a spočítáme jasové statistiky uvnitř elipsoidu. Pomocí takového popisu klasifikujeme oblasti do dvou tříd, jako noduly, nebo jako jiné objekty. Pro klasifikaci používáme jeden lineární a jeden nelineární (prahovací) klasifikátor. Program jsme testovali na 18 vyšetřeních (4853 řezech). Výsledná citlivost samostatných detektorů byla 96%, při 12 falešně pozitivních detekcích/řez. Po klasifikaci klesla citlivost na 89,6% a počet falešně pozitivních na 9/řez. Program byl vyvinut v Matlabu a testován na platformě Windows i Unix.

Prohlášení

Prohlašuji, že jsem svou diplomovou práci vypracoval samostatně a použil jsem pouze podklady (literaturu, projekty, SW atd.) uvedené v příloženém seznamu.

V Praze dne 19.1.2007,



podpis

List of Abbreviations

ANN	Artificial Neural Network
BW	Black and White, binary image
CT	Computed Tomography
DICOM	Digital Imaging and Communication in Medicine
F.e.	For example
FLD	Fisher Linear Discriminant
FN	False Negative
FP	False Positive
GUI	Graphic User Interface
HU	Hounsfield Unit
LoG	Laplacian of Gaussian
STP	Standard Pressure and Temperature
TN	True Negative
TP	True Positive

Contents

1	Introduction	9
1.1	Lung Cancer	9
1.2	Nodules	10
1.3	Tomography	10
1.3.1	Radon Transform	11
1.3.2	Hounsfield Units	12
1.3.3	CT Machines	13
2	Nodule Detection	15
2.1	Problem specification	15
2.2	Previous Work	15
2.2.1	Detection from 2D Data	15
2.2.2	Detection from 3D Data	16
3	Algorithm	19
3.1	Input Data	20
3.2	Lungs Segmentation	20
3.3	Nodule Candidates Finding	20
3.3.1	Parenchymal Nodules	21
3.3.2	Juxtapleural Nodules	21
3.3.3	Summary	23
3.4	Nodule Candidates Clasification	23
3.4.1	Problem Description	24
3.4.2	The Geometrical Model	24
3.4.3	Model Fitting	24
3.4.4	Classifiers	27
4	Methods	29
4.1	Thresholding	29
4.2	BW Morphology	29
4.3	3D Image Filtering	30

4.3.1	Laplacian of Gaussian	30
4.4	Scale Space	30
4.4.1	3D Blob Detector	31
4.5	Iterative Maximization Method	32
4.6	Classification	33
4.6.1	Fisher Linear Discriminant	33
4.6.2	Multiple Thresholding	34
5	Implementation	35
5.1	Requirements	35
5.2	Archive Contents	35
5.3	Control GUI	36
5.3.1	Detection Part of the Dialog	36
5.3.2	Learning Part of the Dialog	37
5.4	Matlab Command Line Interface	38
5.4.1	Detection	38
5.4.2	Learning	38
5.5	Ground Truth Information Reading	39
5.5.1	Drawings Format	39
6	Experiments	41
6.1	Test Data	41
6.2	Evaluation Criteria for Detector Performance	41
6.3	Nodule Candidates Detection	42
6.4	Classification Performance	42
7	Conclusions	47
7.1	Future Work	47
	Image Appendix	49
	Bibliography	59

1 Introduction

1.1 Lung Cancer

Lung cancer is one of the leading causes of death in USA [11] and Europe. Surgery, radiation therapy, and chemotherapy are used in the treatment of lung carcinoma. In spite of that, the five-year survival rate for all stages combined is only 14%. However, early detection helps significantly—it is reported [12] that the survival rate for early-stage localized cancer (stage I) is 49%.

CT is considered to be the most accurate imaging modality available for early detection and diagnosis of lung cancer. It allows detecting pathological deposits as small as 1mm in diameter. These deposits are called lung nodules.

However, the large amount of data per examination makes the interpretation tedious and difficult, leading to a high false-negative rate for detecting small nodules. Suboptimal acquisition parameters (e.g. pitch) further decrease the detection rate. A simulation study demonstrated [1] the overall detection rate to be only 63% for nodules of 1–7 mm in diameter. As the size of the nodule decreased, the sensitivity fell to 48% for nodules smaller than 3mm, and only 1% of nodules smaller than 1.5 mm in diameter were detected. Retrospective analysis of CT scans often shows undetected nodules on the initial scans of oncological patients [2].

Image processing and visualization techniques for volumetric CT data sets may improve the radiologist’s ability to detect small lung nodules. For example, reconstruction of CT images with narrow interscan spacing [3] and interpretation of images using cine rather than film-based viewing technique [4], have been reported to improve small nodule detection.

Computer-assisted tools to improve the detection of small nodules from chest CT are needed and are being actively developed [6].

1.2 Nodules

A solitary pulmonary nodule [36] (parenchymal, non-pleural nodule) is a small, round or egg-shaped lesion in the lungs. Juxtapleural pulmonary nodule is a small, worm-shaped lesion connected to pleura. (Figure 1.1)

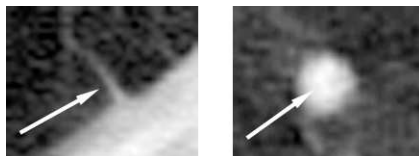


Figure 1.1: Nodule examples: juxtapleural nodule (left), parenchymal nodule (right).

Nodules are typically asymptomatic, and they are usually noticed by chance on a chest X-ray that has been done for another reason. They are usually smaller than 3–4 cm in diameter (no larger than 6 cm) and are always surrounded by normal, functioning lung tissue. Their intensity in CT scans is from -300 to 0 HU

Nodules are fairly common abnormalities on chest X-ray images: nearly one of every 500 chest X-rays shows a newly diagnosed nodules [36]. In the United States, physicians are challenged each year by more than 150,000 new cases. Sixty percent of all nodules are benign. In certain geographical areas where the infectious agents (especially fungi) that cause nodules occur, the percentage of benign nodules increases remarkably (in some areas as high as 90% to 95%). Malignant nodules may be primary lung cancer tumors or metastases from other parts of the body.

If the lesion is suspected to be benign, serial chest X-rays or CT scans may be taken on a regular basis for observation of the lesion. If the affected person is at high risk for lung cancer or if the CT scan appearance of the lesion suggests it is malignant, surgical removal of the lesion is recommended.

1.3 Tomography

Tomography is a method to obtain a cross-sectional images (transversal slices) of given object. In Computed Tomography images of objects (patients) are obtained by X-ray projection [35].

The mathematical basis for tomographic imaging was laid down by Johann Radon (December 16, 1887 (Litoměřice)–May 25, 1956). By applying his theorem slices of human body at various angles can be reconstructed.

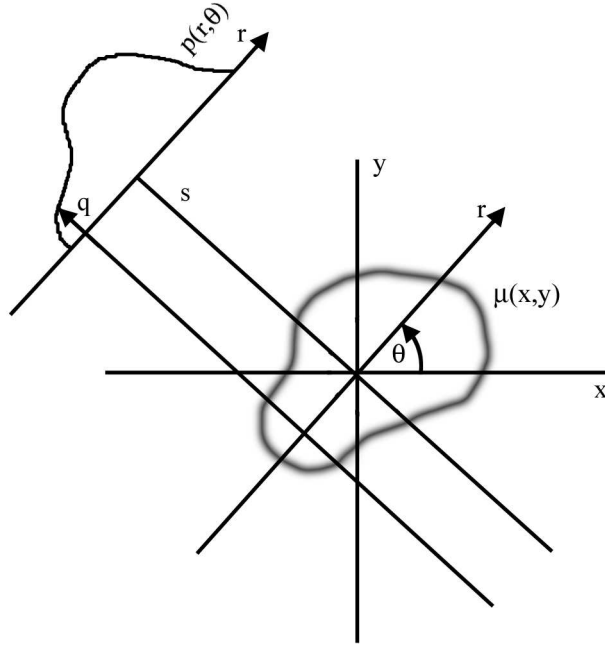


Figure 1.2: Parallel beam geometry. Each projection $p(r, \theta)$ is made up of a set of line integrals through the object $\mu(x, y)$.

In X-ray CT, the line integral represents a logarithm of the total attenuation of the beam of X-rays as it travels in a straight line through the object. The resulting image is a 2D distribution model of the attenuation coefficient $\mu(x, y)$. That is, we wish to find the image $\mu(x, y)$.

1.3.1 Radon Transform

The simplest scanning method is the system of parallel projections, used in the first scanners. We consider the data to be collected as a series of parallel rays, defined by an angle θ and shift r , along the line q defined as

$$x \cos \theta + y \sin \theta = r. \quad (1.1)$$

This is repeated for various angles. Attenuation in tissue occurs exponentially,

$$I = I_0 e^{-\int \mu(x,y) dq}$$

where I and I_0 are output resp. input intensity of ray, $\mu(x, y)$ the attenuation coefficient at position (x, y) along the ray path. The total attenuation of q

Substance	HU
Air	-1000
Nodules	-150
Fat	-180
Water	0
Muscle	40
Bone	1000

Table 1.1: Materials and they radio density in HU

ray at position r , for a projection angle θ , is given by the line integral

$$p(r, \theta) = \ln I/I_0 = \int_q \mu(x, y) ds. \quad (1.2)$$

Using equation (1.1), so the equation (1.2) can be rewritten as

$$p(r, \theta) = \int_{-\infty}^{\infty} \int_{-\infty}^{\infty} \mu(x, y) \delta(x \cos \theta + y \sin \theta - r) dx dy.$$

This transformation is known as the Radon transform [35] (or sinogram) of the 2D object. The projection theorem tells us that if we have all projections of the object

$$p(r, \theta) \text{ where } r \in \mathbb{R}, \theta \in \langle 0, \pi \rangle,$$

we can perfectly reconstruct the original object, $\mu(x, y)$. This is called an inverse Radon transform. It is possible to find an explicit formula for the inverse Radon transform. However, the inverse Radon transform proves to be (extremely) unstable with respect to noisy data. In practice, a stabilized and discretized version of the inverse Radon transform is used, known as the filtered back projection algorithm. (Other reconstruction methods are used, for example based on the Fourier transform).

1.3.2 Hounsfield Units

The intensity of the image in medical X-ray imaging is measured in Hounsfield Units. The scale was established by Sir Godfrey Newbold Hounsfield, one of the principal engineers and developers of computed tomography.

The radio density of distilled water at standard temperature and pressure (STP) is defined as zero Hounsfield Units (HU). The radio density of air at STP is defined as -1000HU. Radio density in HU of air, common tissues and nodules is shown in Table 1.1.

Examination	Typical effective dose [mSv]
Chest X-ray	0,02
Head CT	0,75
Abdomen CT	2,7
Chest CT	3,4
Chest, Abdomen and Pelvis CT	4,9
CT Colonography	3–7
Cardiac CT angiogram	5,5–10

Table 1.2: Typical scan doses per examination

1.3.3 CT Machines

CT machines collect X-ray projections in order to Radon transform (Section 1.3.1). From acquired data reconstruction is computed. the results is an output image showing the distribution of attenuation coefficient $\mu(x, y, z)$ in scanned object represented in HU.

Nowadays CT machines use matrix of detectors to be able to acquire several slices per rotation (32). The X-ray source and detectors makes circular movements around patient, patient moves linearly. Composition of those two movements results in helical movement of source and detectors with respect to the patient. In some machines two X-ray sources and the detector arrays are used for increased examination speed and to lower the dose.

Gantry diameter of a typical CT machine is 78cm, scanning range 200cm, spatial resolution 0.33mm, scanning speed 28mm/sec [33]. Radiation dose received in modern machines is shown in Table 1.2. Typical CT-slice is in Figure 3.3.

2 Nodule Detection

2.1 Problem specification

Nodule detection is an image processing problem. The task is to find positions (and shape) of specific pathological structures in the lungs called nodules. A nodule (Section 1.2) is a small, round lesion in the lungs, or worm-shaped lesion connected to pleura (the lung boundary) with radio-density greather than lung parenchyma. In CT images nodules appear white (Figure 1.1).

Input images (transversal slices) are obtained by tomographic methods (Section 1.3). From CT slices (standartly 512x512pixels) a 3D image (512x512x N) can be assembled. Number N of slices depends on the length of scanning area and on the slice spacing (represented by a parameter called pitch). The spatial resolution in the x and y directions (axes) is typically higher than the resolution in the z axis.

Since our method should be used in medical environment we have tried to fulfill the following requirements:

1. The lowest possible FNs rate (number of missed nodules).
2. Robustness (with respect ot the noise, image resolution, etc.).
3. Relevancy of output (low number of FPs per slice).

2.2 Previous Work

2.2.1 Detection from 2D Data

Chest radiograms are projection images from conventional X-ray. The disadvantage is that on these images ribs, spine and heart may be superposed over nodules, on the other hand, the radiologist (or machine) have to inspect only one image.

Automatic detection of lung nodules is the most studied problem in computer analysis of chest radiographs and almost all methods rely on a two step approach—candidate detection and classification [6]. A lot of methods were developed for the first step, candidate detection: template matching [14], Hough transform [15], subtraction of median filtered image [16], enhancing of nodules by least asymmetric Daubechies wavelet transform and amplifying intermediate levels before back transformation [17]. The second step, classification, is based on: circularity of region, threshold classifier [18], diameter, circularity and irregularity, threshold classifier followed by ANN [19], template matching with nodule and non-nodule candidates, threshold classifier [20].

Comparison between different methods are rare. Sharing databases or setting up common, freely available databases for complete system evaluation has not been, as far as we know, given much attention, yet some databases exists, for example [37]. It contains 247 chest radiographs with 154 nodules.

2.2.2 Detection from 3D Data

3D data from CT machines is considered to be the most accurate imaging modality [5] available for early detection and diagnosis of lung cancer. It allows to detect nodules as small as 1mm in diameter. In CT images of the lungs neither ribs nor heart nor spine decrease diagnostical quality. This is very useful for machine processing. The disadvantage of CT is the large amount of data acquired that makes the interpretation for human radiologist difficult and increases the time of machine processing. Also the price of machine and higher dose recieved during examination is disadvantage of CT.

There are many projects in CT image processing dealing with nodule detection. They can be divided into two groups of approaches: density-based and model-based approaches. Density-based detection methods employ techniques such as multiple thresholding [21, 22, 23], region-growing [24], locally adaptive thresholding in combination with region-growing [25] and fuzzy clustering [26] to identify nodule candidates in the lungs. For the model-based detection approaches, the relatively compact shape of a small lung nodule is taken into account while establishing the models to identify nodules in the lungs. Techniques such as "N-Quoit filter" [27] template-matching [28], object-based deformation [29] and the anatomy-based generic model [30] have been proposed to identify sphere-shaped small nodules in the lungs. Other attempts include automated detection of lung nodules by analysis of curved surface morphology [31] and improvement of the nodule detection by subtracting broncho-vascular structures from the lung images [32].

Due to the relatively small size of the existing CT lung nodule databases

[38] and the various CT imaging acquisition protocols, it is hard to compare the detection performance among the developed algorithms. Also differences in specifications of the nodules make the comparison hard. (For example, if algorithm detects nodules 2–10mm in diameter, than 1mm nodules are not FNs, but if nodule specification is 1–10mm, they are.)

3 Algorithm

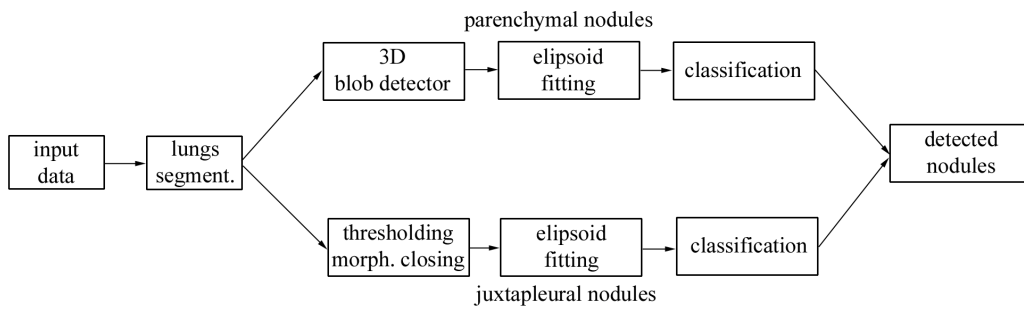


Figure 3.1: Overall scheme of nodule detection algorithm. Lungs segmentation is common for juxta-pleural and parenchymal nodules, next steps are separated. For parenchymal nodule candidates detection, the multi scale 3D blob detector is applied, for detection of juxta-pleural nodule candidates thresholding and methods of mathematical morphology are used. Finally each nodule candidate is described by its shape and intensity parameters and classified.

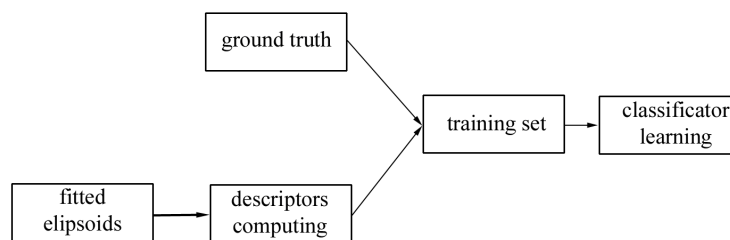


Figure 3.2: Overall scheme of classifier learning. Training set consists of descriptors of detected nodule candidates, ellipsoid model fitted on them and ground truth information.

Our fully automatic nodule candidate detection algorithm uses thresholding-based segmentation, blob detector using multiscale LoG filters with post processing for parenchymal nodule candidates detection, and mathematical morphology tools for juxtapleural nodule candidates detection. Next step consists of applying an automatic nodule classification system, based on geometrical and image features, to the candidates. We have tested a linear classifier and a classifier based on thresholding.

Nodule candidates detectors are designed to have a good sensitivity and few false negatives, classifiers have to decrease the number of false positive results.

3.1 Input Data

The input is a 3D grayscale volume data from one examination of one patient. Grayscale values are not in HU, but can be converted. We work internally with machine intensity values. All values of intensity given here will be in HU. Conversion coefficients from machine intensity levels to HU are different for each machine.

3.2 Lungs Segmentation

Lungs can be easily separated from other anatomic structures by binary thresholding (Section 4.1) at $-350HU$ (Figure 3.5a)

$$m_1(x, y, z) = Thr(f(x, y, z); -350HU).$$

On Figure 3.3 you can see lighter tissue (fat and muscle) around the lungs, on Figure 3.4 is a histogram of the same image.

After thresholding, the background (the outside of the body) is eliminated by suppressing all components adjacent to image edges by flood-filling. This gives us a lung mask $m(x, y, z)$ (1 as lungs, 0 background) (Figure 3.5b)

3.3 Nodule Candidates Finding

Both types of nodules, juxtapleural and parenchymal, are high density objects (in CT images appear as bright). Because of a big difference in shape, we have decided to perform detection of these two classes independently.

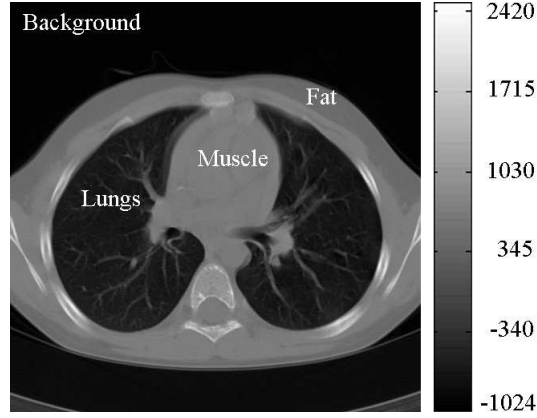


Figure 3.3: Original CT slice and tissues localization. Intensity values are given in HU.

3.3.1 Parenchymal Nodules

Input of a parenchymal nodule detector is a 3D image $f(x, y, z)$ and the lung mask $m(x, y, z)$ from segmentation. For better results the lung mask is smoothed (Figure 3.5c) by morphological closing (Section 4.2) with spherical element 9mm in diameter

$$e(x_0, y_0, z_0) = \begin{cases} 1 & \text{for } \sqrt{(x - x_0)^2 + (y - y_0)^2 + (z - z_0)^2} \leq 4.5mm \\ 0 & \text{else.} \end{cases}$$

The values in pixels are different. The smoothed mask is then:

$$s(x, y, z) = m(x, y, z) \bullet e(x, y, z)$$

Image $f(x, y, z)$ is multiplied by the smoothed mask $s(x, y, z)$ element by element

$$g(x, y, z) = f(x, y, z) \cdot s(x, y, z).$$

From the segmented lungs image a nodule candidates are detected by a multiscale 3D blob detector (Section 4.4).

3.3.2 Juxtapleural Nodules

This part of the detector works on each slice separately, because of almost no regularity of the juxta-pleural nodules in the z-direction.

The detector operates on the smoothed mask $s(x, y, z)$ and the original image $f(x, y, z)$ thresholded at -600HU (Section ??)

$$t(x, y, z) = Thr(f(x, y, z); -600HU).$$

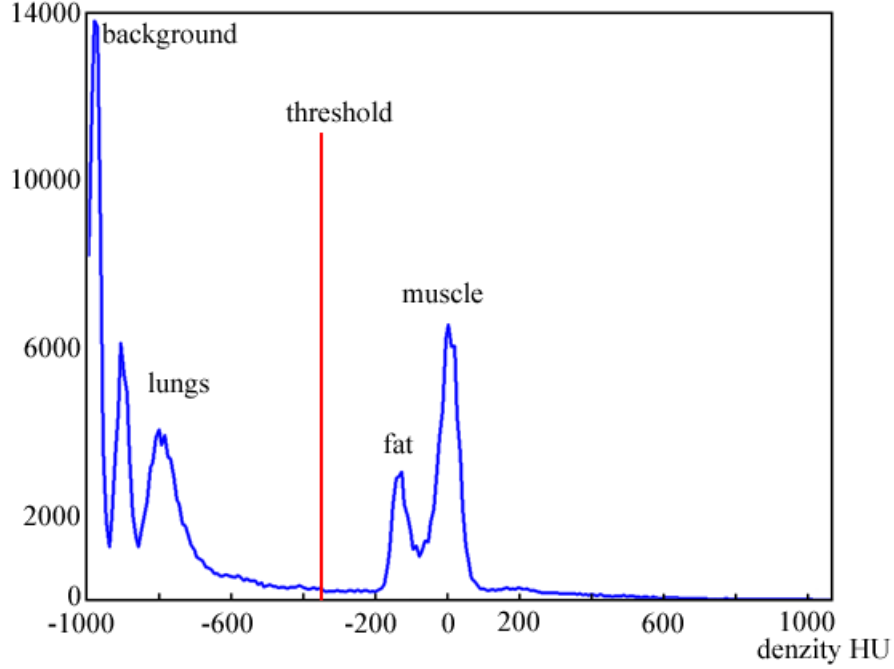


Figure 3.4: Histogram of the image in Figure 3.3 and the segmentation threshold (red).

This threshold level is different from segmentation threshold because now we need a lot of information from lung edge, and in time of segmentation we needed lung mask without holes.

High density nodules appear as zero-valued (black) irregularities on the lung edges (Figure 3.6a) after thresholding, so subtraction of the thresholded image $t(x, y, z)$ and the smoothed mask $s(x, y, z)$ shows them well

$$j_0(x, y, z) = s(x, y, z) - t(x, y, z).$$

In the next step objects not located on lung boundary are eliminated from $j_0(x, y, z)$ by the following procedure.

Lungs boundary is generated from the smoothed mask by morphological eroding and subtracting

$$b(x, y, z) = s(x, y, z) - (s(x, y, z) \ominus e_1(x, y, z)),$$

where e_1 is disc element of 2.5mm in diameter (Figure 3.6b). The mask $j_0(x, y, z)$ is then multiplied element by element by boundary mask $b(x, y, z)$

$$j(x, y, z) = g(x, y, z) \cdot b(x, y, z).$$

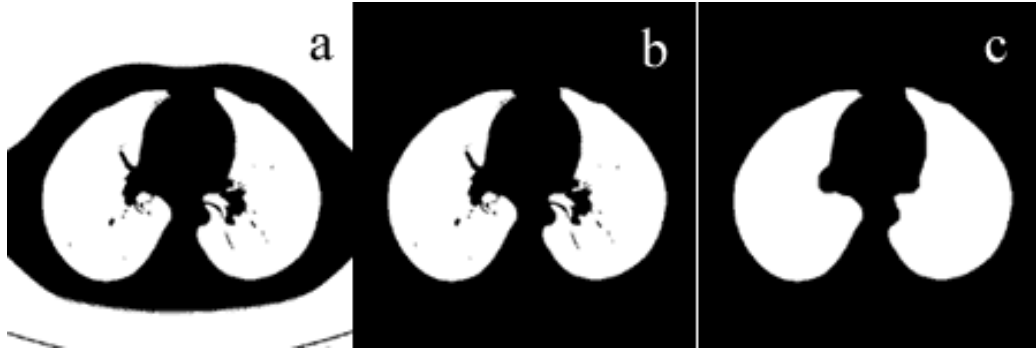


Figure 3.5: Progress of lung mask generation: (a) thresholding, (b) flood filling, (c) smoothing.

Finally, large objects (greater than 29mm^2) in each slice are eliminated because of small expected dimensions of juxtaleural nodules (Figure 3.6c).

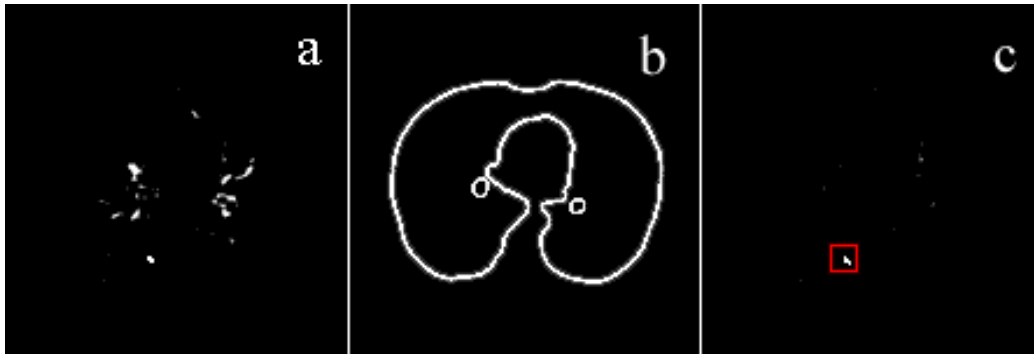


Figure 3.6: Juxtaleural nodule detection: (a) mask $j_0(x, y, z)$, (b) lung edge $b(x, y, z)$ (c) small object on an edge.

3.3.3 Summary

As early testing (Section 6.3) shows, our detectors work well. Sensitivity of detectors is about 96%. FPs rate about 12 FPs per slice. In the next Section we show how to get better results (decrease number of FPs) by using classifiers.

3.4 Nodule Candidates Clasification

Output from detectors are two sets of pixels P from parenchymal and J from juxtaleural. Each pixel of those sets is probable center of a nodule. Both

sets are processed by classifiers described below.

3.4.1 Problem Description

Classification divides candidate points from parenchymal ($\mathbf{p} = (p_x, p_y, p_z) \in P$) and juxta-pleural ($\mathbf{j} = (j_x, j_y, j_z) \in J$) detectors to two classes: nodule and non-nodule. Ideally, the classifier should correctly detect all true nodules, and also correctly reject all non-nodules. This leads to a decrease of the number of FP results with constant number of TPs.

Our classifiers are trying to separate classes one from each other (linear classifier base on FLD), or cut of candidates with a far values of description (multi-threshold classifier).

3.4.2 The Geometrical Model

Points from detectors (Sections 3.3.1 and 3.3.2) are described by their centers \mathbf{p} and \mathbf{j} . For successful classification, more descriptor features than only a center are needed. We will classify each nodule candidate according to its shape. To describe nodules we choose an ellipsoid model

$$E = \left\{ f(x, y, z) : \frac{(x - x_0)^2}{a^2} + \frac{(y - y_0)^2}{b^2} + \frac{(z - z_0)^2}{c^2} \leq 1; \mathbf{x} = (x_0, y_0, z_0) \in X \right\}.$$

further rotated by angles φ and ϑ around coordinate axes.

Parameters of the ellipsoid model E are $a, b, c, \varphi, \vartheta$, and we will consider them as a vector $\mathbf{s} = (a, b, c, \varphi, \vartheta)$. The center (x_0, y_0, z_0) of the ellipsoid E is optimized independently (see Section 3.4.3).

3.4.3 Model Fitting

Exact Center Specification

First we find the center (x_0, y_0, z_0) of the future ellipsoid. We need to do it, because the nodule candidate center (x_c, y_c, z_c) obtained either from parenchymal or juxtapleural nodule candidates detectors is not accurate enough.

We proceed it as follows: We take a cube neighborhood

$$c_1(x_c, y_c, z_c) = \{(x, y, z) : x - x_c + y - y_c + z - z_c \leq 7mm\}$$

of each $\mathbf{x} \in X$ and threshold it at -720HU (Figure 3.7b)

$$o(x, y, z) = T_{hr}(f(x, y, z); -750HU), (x, y, z) \in c_1.$$

Nearest object in the sense of Euclidean distance (pixel of value 1) to \mathbf{x} in $o(x, y, z)$ is found. All other objects (not connected to the nearest one) are eliminated from $o(x, y, z)$. Center of the single object now present in $o(x, y, z)$ is localized by repeatable morphological erosion by 3D structural element created as 6-neighbourhood of center pixel, until the object disappears.

We take the improved center \mathbf{x} from last nonempty eroding step, as its center of mass. Number of erosions is a first estimation (r) of the radius of the ellipsoid. (Figure 3.7c).

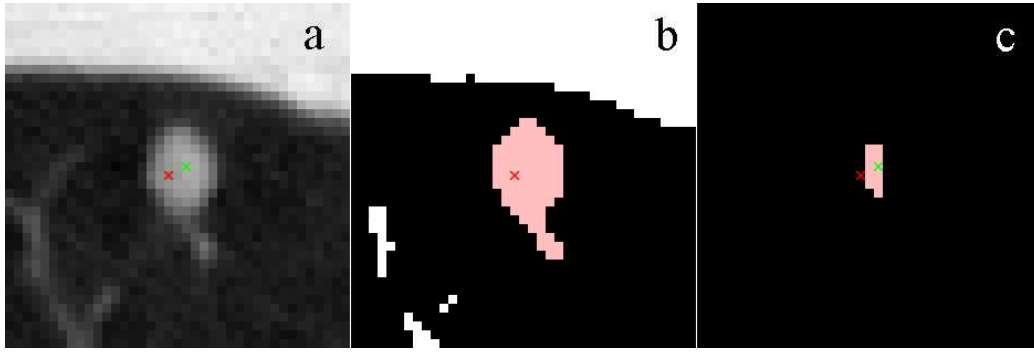


Figure 3.7: 2D example of a center specification process. Red cross—old center, green cross—improved center. (a) Neighbourhood of old center, also improved center displayed. (b) Thresholded neighbourhood and the object nearest to the old center (light red). (c) Neighbourhood after erosion. New center is marked by a green cross. The radius estimation $r = 3$.

Intensity Threshold Finding

Once the center \mathbf{x} is known, we will find a threshold T . We define a new cubical neighbourhood

$$c_2(x_0, y_0, z_0) = \{(x, y, z) : x - x_0 + y - y_0 + z - z_0 \leq r + 6\text{pixels}\}$$

\mathbf{x} and cut it along coordinate axes (Figure 3.8 top) as follows

$$\begin{aligned} f_x(x) &= f(x, 0, 0) \\ f_y(y) &= f(0, y, 0) \\ f_z(z) &= f(0, 0, z) \end{aligned}$$

and find the position of the maximum and minimum derivatives along each cut.

$$gf_x(x) = \frac{df(x)}{dx}$$

$$gf_y(y) = \frac{df(y)}{dy}$$

$$gf_z(z) = \frac{df(z)}{dz}$$

(Figure 3.8 bottom). The threshold T is computed as the mean intensity of voxels at the positions of the maximum derivatives.

$$T = \frac{I_{x+} + I_{x-} + I_{y+} + I_{y-} + I_{z+} + I_{z-}}{6}.$$

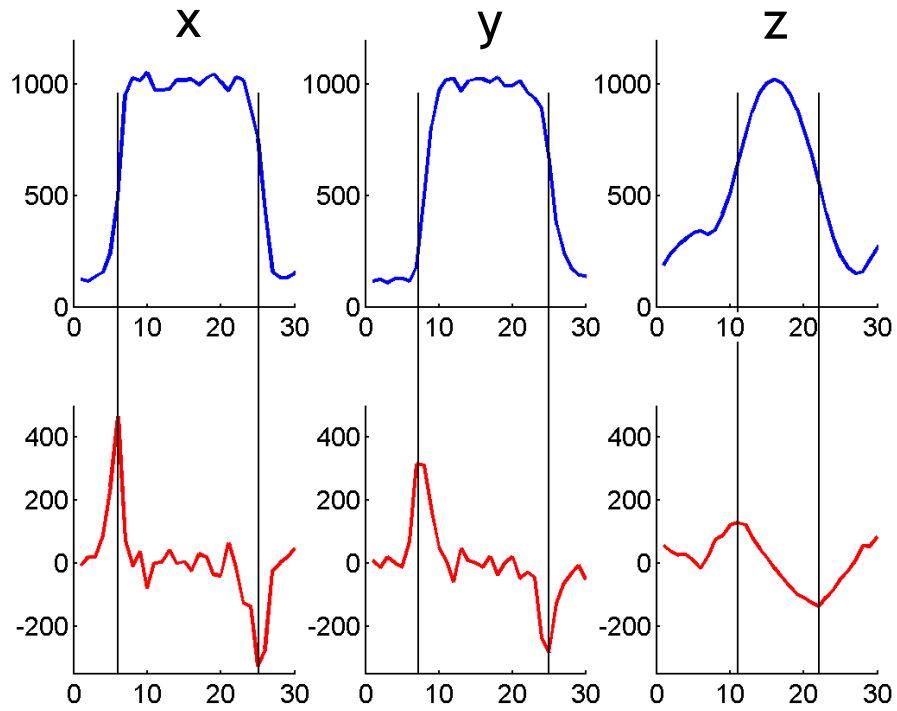


Figure 3.8: Intensity profiles f_x , f_y , f_z of nodule along coordinate axes (top) and correspondent derivatives (bottom)

Ellipsoid Parameters Fitting

The parameters $\mathbf{s} = (a, b, c, \varphi, \vartheta)$ of the ellipsoid are found by maximization of a criterion

$$J(\mathbf{s}) = \sum_{(x,y,z) \in E} f(x, y, z) - T. \quad (3.1)$$

By maximizing J we are looking for ellipsoid which contains as many pixels as possible with intensity greater than T , and every pixel with intensity less than T in ellipsoid is penalized. The iterative method is used (Section 4.5). Initial guess is

$$\begin{aligned} a, b, c &= r + 3 \\ \varphi &= 0 \\ \vartheta &= 0. \end{aligned}$$

Examples of fitted ellipsoids are in Figure 7.1.

3.4.4 Classifiers

Two classifiers were tested. First, a simple multi-threshold classifier. Second, a linear classifier based on Fisher linear discriminant. (See Section 4.6 for details.) For both classifiers the same eight input shape descriptors of each nodule are used [41]:

effective radius	$d_1 = \sqrt[3]{abc}$
discircularity	$d_2 = \max(a, b, c) - r_{ef}$
elongation	$d_3 = \frac{\max(a,b,c)}{\min(a,b,c)}$
mean intensity	$d_4 = \sum_{(x,y,z) \in E} f(x) / \text{number of pixels} \in E$
intensity sum	$d_5 = \sum_{(x,y,z) \in E} f(x)$
number of pixels	$d_6 = \text{number of pixels} \in E$
variance of intensity	$d_7 = \text{var}(\{f(x, y, z) : (x, y, z) \in E\})$
threshold	$d_8 = \text{the intensity threshold } T$

Output of both classifiers is one of two classes: 'nodule', or 'not nodule' for each input vector $\mathbf{d} = (d_1, d_2 \dots d_8)$. Input data for classifiers learning are acquired by ellipsoid fitting procedure, see Section 3.4.3. Classifiers and their learning is described in Section 4.6.

4 Methods

4.1 Thresholding

Binary thresholding [9] is the transformation of grayscale image f to binary(BW) image g as follows

$$g(x, y, z) = Thr(f(x, y, z); T) = \begin{cases} 0 & \text{for } f(i, j) \geq T \\ 1 & \text{for } f(i, j) < T. \end{cases}$$

4.2 BW Morphology

In binary morphology [9] we have a point set X and a structure element A , represented by coordinates of white image pixels (in BW image we have only black or white pixels).

The morphological dilatation of X by the structural element A is an union of shifted point sets

$$Y = X \oplus A = \bigcup_{a \in A} X_a.$$

Dilatation is used to expand the object X in a way controlled by the structure element A .

The morphological erosion of X by the structural element A is an intersection of all translations of the image X by the vector $-a \in A$. Erosion is used to reduce object in a way controlled by the structure element A .

$$Y = X \ominus A = \bigcap_{a \in A} X_{-a}.$$

The morphological opening of X by the structural element A is

$$Y = X \circ A = (X \ominus A) \oplus A.$$

Opening enlarges 'holes' in the objects in a way controlled by the structure element A .

The morphological closing of X by the structural element A is

$$Y = X \bullet A = (X \oplus A) \ominus A.$$

Closing fills 'holes' in objects in a way controlled by the structure element A .

4.3 3D Image Filtering

3D filtration of image f by a 3D filter h is a discrete convolution [9]

$$a(i, j, k) = h * f = \sum_{m, n, o} h(i - m, j - n, k - o) f(m, n, o).$$

If the filter h is separable, i.e.

$$h(m, n, o) = h_m(m) \times h_n(n) \times h_o(o)$$

the convolution can be separated to three 1D operations

$$a(i, j, k) = h_m *_{m} \left(h_n *_{n} \left(h_o *_{o} f(m, n, o) \right) \right)$$

which accelerates significantly the filtration process.

4.3.1 Laplacian of Gaussian

LoG [7] is convolutional kernel (filter) l created from Gaussian kernel

$$g(x, y, z, \sigma) = \frac{1}{2\pi\sigma} e^{-\frac{x^2+y^2+z^2}{2\sigma}},$$

by applying a Laplacian operator

$$l(x, y, z, \sigma) = \nabla^2 g(x, y, z, \sigma).$$

Separability of the LoG filter is used to accelerate scale filtering.

4.4 Scale Space

Scale space [7] theory is a framework for multi-scale image representation. It is a formal theory for handling image structures at different scales and how a scale parameter σ can be associated with each level in the scale-space representation.

In this text scale space is represented by four 3D scale images—input image $f(x, y, z)$ filtered by LoG filters with diameter $d_k=5.5, 8, 10,$ and 12.5mm . These diameters cover all the range of typical dimensions of nodules. The relationship between diameter d_k and variance σ_k of each filter [39] is

$$\sigma_k^2 = \left(\frac{d_k - 1}{3} \right)^2.$$

Parameter σ_k (or d_k) of each LoG filter is associated with one scale (Figure 4.1).

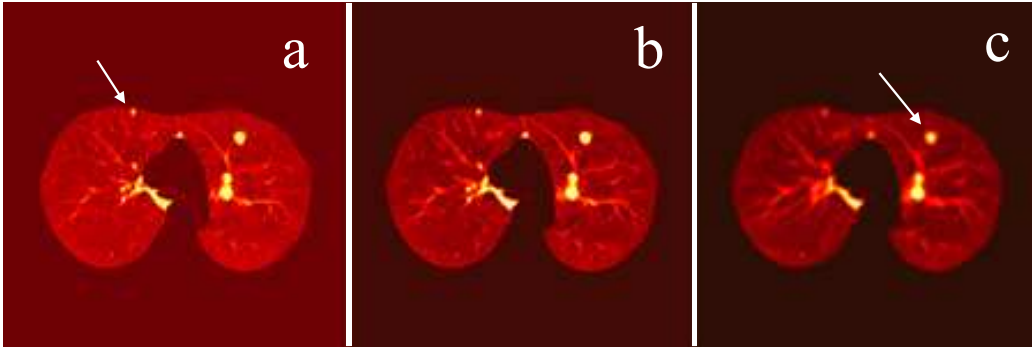


Figure 4.1: One slice in scale space (a) $\sigma = 1.5$, (b) $\sigma = 2.3$, (c) $\sigma = 3.8$. Small nodule is best localized in image (a) large nodule in image (c).

4.4.1 3D Blob Detector

Blob detector [7] is a filtration algorithm which is used for detection of spherical object in images. One of the first, and also the most common blob detector is based on the LoG filter. Input image is filtered by a 3D LoG filter.

After creating the scale space (Section 4.4)

$$s_k(x, y, z) = f(x, y, z) * l_{\sigma_k}(x, y, z), \quad k = 1 \dots 4,$$

local maximas in each scale image $s_k(x, y, z)$, are found. It means creating of local maxima maps $m_k(x, y, z)$. Pixels with value greater than all pixels in they 26-neighborhood $n_{26}(x, y, z)$ are set to 1. Every other pixel is set to 0.

$$m_k(x, y, z) = \begin{cases} 1 & \text{if } s_k(x, y, z) = \max(n_{26}(x, y, z)) \\ 0 & \text{else.} \end{cases}$$

Local maxima is then traced from $m_1(x, y, z)$ to $m_4(x, y, z)$ by morphological dilatating and multiplication. For example, map $m_1(x, y, z)$ is dilatated (Section 4.2) by a structure element

$$e(x, y, z) = \left\{ (x, y, z); x^2 + y^2 \leq \begin{cases} 5.4mm; & z = 0 \\ 1.2mm; & |z| < 1 \end{cases} \wedge |z| \leq 1 \right\}$$

and multiplied element-wise with map $m_2(x, y, z)$

$$m_{x1}(x, y, z) = (m_1(x, y, z) \oplus e(x, y, z)) \cdot m_2(x, y, z).$$

In other words, if some maxima from $m_2(x, y, z)$ is in the $e(x, y, z)$ -neighbourhood of points from $m_1(x, y, z)$, is retained to the next step, every other maxima is thrown away.

Next steps are analogous to a first one:

$$m_{xk}(x, y, z) = (m_{xk-1}(x, y, z) \oplus e(x, y, z)) \cdot m_k(x, y, z)$$

As result, in $m_{x4}(x, y, z)$ we have stable maximas, which do not significantly change position between scales. These points are interpreted as potential parenchymal nodule centers.

4.5 Iterative Maximization Method

Our maximization (iterative coordinate ascent) method consists of steps and iterations. In each step, only one of five parameters $\mathbf{s} = (a, b, c, \varphi, \vartheta)$ is changed and a new value of the criterion is J computed (3.1). If the value of J increases, the step is finished, the parameter is fixed, and the next step starts. Each five steps (for five parameters) we call an iteration.

We define for convenience:

$$\mathbf{s}(a, b, c, \varphi, \vartheta) = \mathbf{s}(s_1^{i_1}, s_2^{i_2}, \dots, s_5^{i_5})$$

and from (3.1)

$$J^i = J(\mathbf{s}^i),$$

where i_n resp. i is 0 or 1, old value, or optimized value of n -th parameter, resp. J .

In the n -th step of each iteration the value of the n -th parameter s_n^0 is decreased by $s_n^0/2^k$ where $k = 1$

$$s_n^1 = s_n^0 - \frac{s_n^0}{2^k}.$$

If the value of J decreases,

$$J^1 \leq J^0$$

new value of parameter

$$s_n^1 = s_n^0 + \frac{s_n^0}{2^k}.$$

is tested. If $J^1 \leq J^0$, the value of k is increased ($k = 2$) and so on until J increases, or $k = 4$. Then $n + 1$ -th step of the iteration starts.

If value of J does not change during the iteration, the maximization process ends.

We chose this method, because of problems with methods standarty implemented in Matlab.

4.6 Classification

Classifier [9] is a device with n inputs and one output. Inputs are represented by input vector $\mathbf{x} = (x_1, \dots, x_n)$. An R -class classifier will generate one of R class symbols $\omega_1 \dots \omega_R$ as an output. We are using a 2-class classifier with output $y \in \{\text{'nodule'}, \text{'not nodule'}\}$.

The function $d(\mathbf{x}) = y$ is called a decision rule. Class of decision rule is given by classifier design, parameters by learning process. The input to the learning process is a set $T = \{(x_1, y_1), \dots, (x_l, y_l)\}$ of binary labeled $y_i \in \{1, 2\}$ training vectors $\mathbf{x}_i \in \mathbb{R}^n$. Let $I_y = \{i : y_i = y\}, y \in \{1, 2\}$ be sets of indices of training vectors belonging to the first $y = 1$ and the second $y = 2$ class. Each decision rule can be described by R discrimination functions. If all R discrimination function are linear, classifier is called linear.

4.6.1 Fisher Linear Discriminant

Classifier based on FLD [34] uses one linear discrimination function

$$g(\mathbf{x}) = b + q_1 x_1 + \dots, q_n x_n,$$

if the value of discrimination function is positive, input vector is classified into first class, if it is negative into second class. This classifier parameters are set to maximize the class separability. The class separability in a direction $\mathbf{q} \in \mathbb{R}^n$ is defined as

$$F(\mathbf{q}) = \frac{\langle \mathbf{q} \cdot \mathbf{S}_B \mathbf{q} \rangle}{\langle \mathbf{q} \cdot \mathbf{S}_Q \mathbf{q} \rangle}, \quad (4.1)$$

where \mathbf{S}_B is the between-class scatter matrix

$$\mathbf{S}_B = (\boldsymbol{\mu}_1 - \boldsymbol{\mu}_2)(\boldsymbol{\mu}_1 - \boldsymbol{\mu}_2)^T, \quad \boldsymbol{\mu}_y = \frac{1}{|I_y|} \sum_{i \in I_y} \mathbf{x}_i, y \in \{1, 2\},$$

and \mathbf{S}_Q is the within class scatter matrix defined as

$$\mathbf{S}_Q = \mathbf{S}_1 + \mathbf{S}_2, \quad \mathbf{S}_y = \sum_{i \in Y_y} (\mathbf{x}_i - \boldsymbol{\mu}_y)(\mathbf{x}_i - \boldsymbol{\mu}_y)^T, y \in \{1, 2\}.$$

In the case of the FLD, the parameter vector \mathbf{q} of the linear discriminant function $g(x) = \langle \mathbf{q} \cdot \mathbf{x} \rangle + b$ is determined to maximize the class separability criterion (4.1)

$$\mathbf{q} = \arg \max_{\mathbf{q}'} F(\mathbf{q}'), \quad (4.2)$$

which is equivalent to the generalized eigen value problem [8]

$$\mathbf{S}_B \mathbf{q} = \lambda \mathbf{S}_Q \mathbf{q}.$$

The problem (4.2) can be solved by the matrix inversion

$$\mathbf{q} = \mathbf{S}_Q^{-1}(\boldsymbol{\mu}_1 - \boldsymbol{\mu}_2).$$

The bias b of the linear rule must be determined based on another principle, by solving equality

$$\langle \mathbf{q} \cdot \boldsymbol{\mu}_1 \rangle + b = -(\langle \mathbf{q} \cdot \boldsymbol{\mu}_2 \rangle + b),$$

since we consider the same distance of b from each class.

4.6.2 Multiple Thresholding

A very simple nonlinear classifier is based on multiple thresholding. The decision rule uses $2n$ thresholds where n is number of descriptors.

If all elements of input vector are between corresponding thresholds, vector is classified as 'nodule', if not, as 'not nodule'

$$y = \begin{cases} \text{'nodule'} & \forall k \in \{1, \dots, 8\}; l_k \leq x_k \leq h_k \\ \text{'not nodule'} & \text{else,} \end{cases}$$

where l_k, h_k are low and high thresholds.

Learning consists of searching the biggest and the smallest value of each parameter in $P_y = \{\mathbf{x}_i : y_i = 1\}$ from the training set.

5 Implementation

The algorithm was implemented in the Matlab. It is divided into functions and controlled by a single GUI.

5.1 Requirements

The software was developed in Matlab 6.5. under Windows system. Besides standard functions of Matlab and Matlab Image Processing Toolbox, we use also Statistical Pattern Recognition Toolbox [34]. For the ability to running on a Unix system some parts of the code had to be changed. Now the program runs on both systems, but further problems are possible on the Unix platform.

Because of large amount of data processed, we recommend computers with at least 4GB of RAM. Speed of the processor is not crucial.

Simple GUI available to control the functions of the program, also Matlab shell can be used. We recommend to control the program from the GUI.

5.2 Archive Contents

Part of this work is data archive which contains whole program, small data set with ground truth, two learned classifiers (FLD and multi-threshold), electronic version of this text and three miscellaneous scripts.

List of contents:	
noduledet.pdf	This text in pdf format.
noduledet.ps	This text in post script format.
readme.txt	Archive description.
Code/	Directory containing whole Matlab program.
Code/countquad3.m	Evaluates maximized criterion J .
Code/lapofgau.m	Creates LoG filters.
Code/maskquad3.m	Creates BW mask of ellipsoid.
Code/nodcllearn.m	Learns classifiers.
Code/nodclparam.m	Computes shape description of nodules.
Code/nodfitting.m	Fits ellipsoids on to nodule.
Code/nodgui.m	Control GUI.
Code/noduledet.m	Detect nodule candidates
Code/Misc/clasif.m	Classifies precomputed data.
Code/Misc/fastlearn.m	Learns classifiers from precomputed data.
Code/Misc/noduledetcode.m	Precomputes data.
Data/	Directory containing testing data.
Data/Drawings/	Directory containing ground truth information.
Data/Exams/	Directory containing examinations.
Data/LearnedClass/FLDall.mat	FLD based classifiers learned from all suitable exams.
Data/LearnedClass/FLDall.mat	Multi-threshold classifiers learned from all suitable exams.

5.3 Control GUI

GUI is started by typing `nodgui` in Matlab command window.

The interface is separated to two parts by a radiobutton. The first part contains everything about detection, the second about classifier learning. After setting the directories and files start the process by pushing the "Detect" or "Learn" buttons respectively.

5.3.1 Detection Part of the Dialog

The expected content of the input fields shown in Figure 5.1 is as follows:

CT set: directory where examination is located, see Figure 5.3. In the directory the examination can be divided to three or five subdirectories. The first one (in alphabetical order) contains frontal images of the patient (usually 2). Second and third subdirectories contain the examination. If fourth and fifth subdirectories are also present, they contain the same examination acquired with greater pitch parameter.

Output: directory to which the results are saved. The name of the output '.mat' file consists of the last five letters of the CT set name.

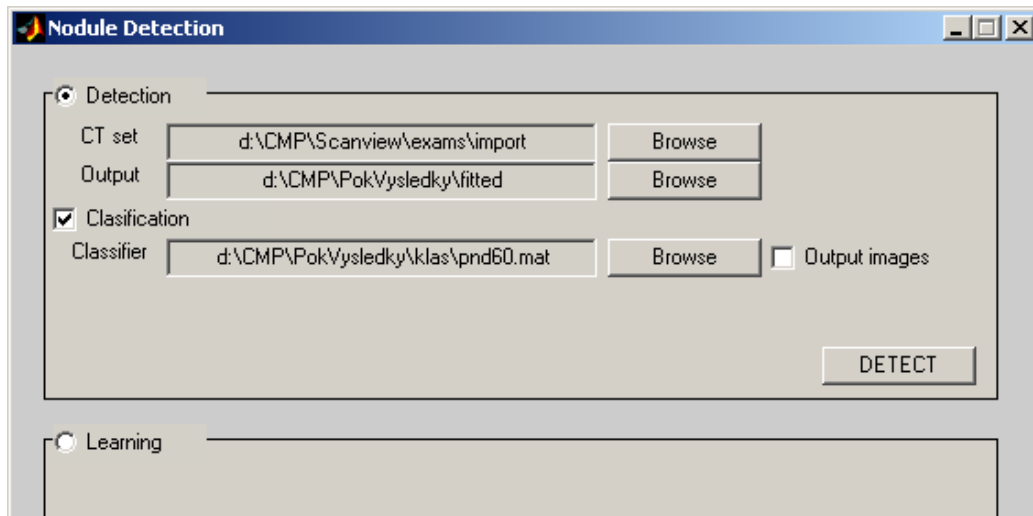


Figure 5.1: Upper part of the GUI used for nodule detection.

Classifier: file contains classifier parameters. It is created by the learning part.

Classification: turns on/off fitting and classification process. If not set, no classifier will be applied and all nodule candidates are reported. The process is much faster, but not so precise (many of FPs) and there is no information about nodule shape. It is useful for example if no classifier is available.

Output images: turns on/off saving '.jpg' images besides '.mat' file to the same directory.

Example of the directory structure is in Figure 5.3.

5.3.2 Learning Part of the Dialog

The expected content of input fields shown in Figure 5.2 is as follows:

Training set: directory with one or more '.mat' files containing information about detected nodules. Name of files have to correspond to examination subdirectory names. This directory may not contain anything else.

CT sets: directory containing all available exams in separate subdirectories.

Drawings: contains subdirectories with Scan View drawings (ground truth) as described in Section 5.5.

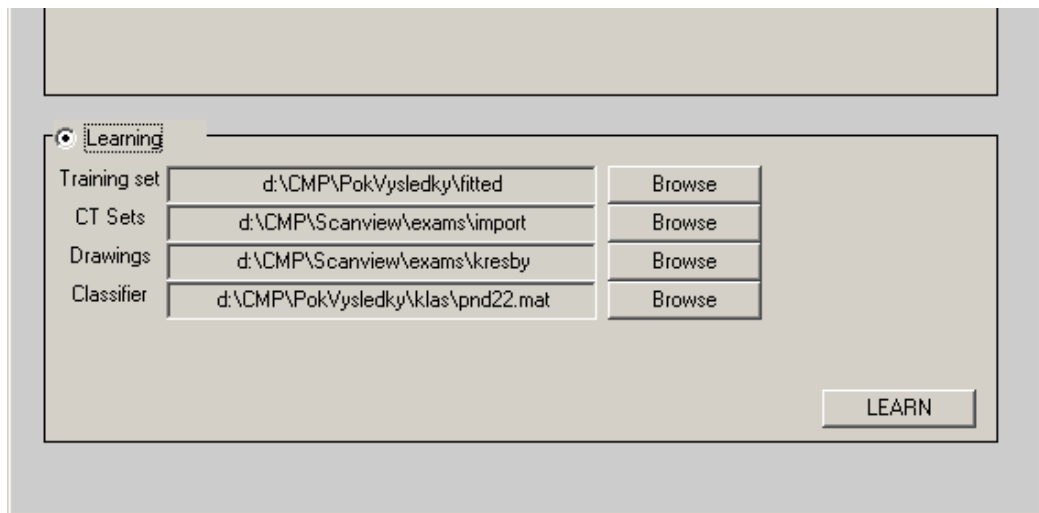


Figure 5.2: Lower part of the GUI used for classifier learning.

Classifier: output file with classifiers parameters.

See the example of the directory structure in Figure 5.3.

5.4 Matlab Command Line Interface

5.4.1 Detection

Nodule detection function

```
noduledet(CTset, Output, [], Classifier, Classification, [], [], [], OutputImages)
```

The expected content of the parameters is the same as described in Section 5.3.1, with the following Matlab types:

`CTset`, `Output`, `Classifier`—char array,

`Classification`, `OutputImages`—logical.

Function has the same effect as when the "DETECT" button is pressed.

5.4.2 Learning

For classifier learning function

```
nodulecllearn(TrainingSet, CTsets, Drawings, Classifier)
```

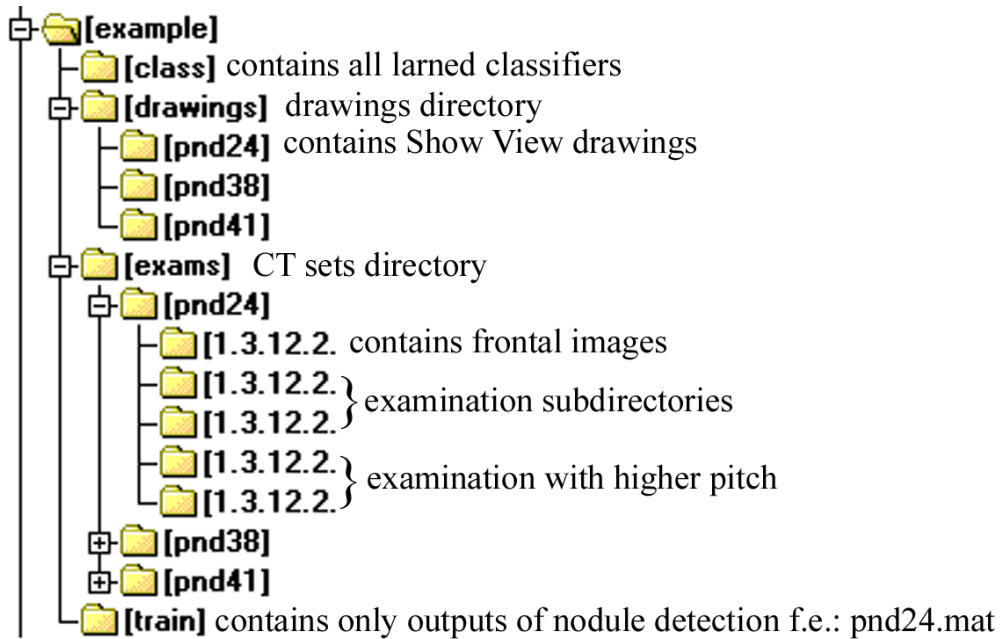



Figure 5.3: Example of directory structure expected by the program.

The expected content of the parameters is the same as described in Section 5.3.2, all input parameters are char arrays.

Function has the same effect as when the "LEARN" button is pressed.

5.5 Ground Truth Information Reading

Ground truth information about nodules was created in Scan View, program by RNDr. Jan Krásenský (jkras@lf1.cuni.cz). Scan View allows to add drawings of many kinds into each slice of exam. For this work only circle drawings were used, because of easy machine reading of simple shapes. If some examiner used more precise selecting of nodules, his drawings were manually changed to circles.

5.5.1 Drawings Format

To allow Scan View link drawings and examinations together, directory name of drawings and exams must be the same. If there are no drawings present, directory is created automatically.

Scan View also creates a single file for each slice containing one or more drawings with the same name as the slice. Those files combines ASCII and binary values to describe drawings on slice.

Reading of files is not very easy because of neither official nor unofficial documentation to file format exists. Table 5.1 shows some structures used in this work, gained during oral consultations with Scan View author.

Starting Byte	Length [Bytes]	Description
1	2	Drawing header ASCII, 'ZJ' for circles
452	4	500000x coordinate of center [pixels]
456	4	500000y coordinate of center [pixels]

Table 5.1: Structures used from Scan View drawings files. (Field meanings might be different in non circle drawings. Structure repeats periodically after 2880Bytes.)

6 Experiments

6.1 Test Data

Our test data consist of 18 CT volume scans (18 patients, 4853 slices) for which ground truth nodule information was available. In total, there were 222 known nodules, 74 juxtapleural and 148 parenchymal. All data was acquired on Somatom AR Star CT machine (Siemens). Resolution of images was 1.6pixels per mm.

Our ground truth information are nodules signed by expert by circles in program Scan View. Information readed from Scan View drawing files (Section 5.5) was interpreted as set of centers of mass of each nodule in each slice. This information is differently processed for parenchymal and juxtapleural nodules, because of low regularity of juxta-pleural nodules. For parenchymal nodules, center of mass of the ground truth nodule is computed from nodule circle cenders in all slices containing the nodule. For juxtapleural nodules we leave centers in all slices, because juxta-pleural nodules are detected slice-wise.

6.2 Evaluation Criteria for Detector Performance

Our detector (see Sections 3.3.1 and 3.3.2) and classifiers (Section 3.4) provide for each detected nodule the coordinates of its center $\mathbf{x} = (x, y, z)$. If the distance between the detected point $\mathbf{x} = (x, y, z)$ and closest ground truth point $\mathbf{g} = (x, y, z)$ is smaller than 3mm

$$|\mathbf{x} - \mathbf{g}| \leq 3mm,$$

nodule is considered as correctly detected and counted as a true positive result (TP). Every other detected point is considered as false positive (FP). If there is no point detected in a 3mm neighbourhood of the ground truth, the point is considered as false negative (FN). We also define true negative results

(TN) as FP points detected by nodule candidates detectors and classified to class 'not nodule' by a classifier.

We have calculated the following statistics:

FPS/slice: the average number of FPs per slice

Sensitivity: Number of detected nodules to total number of nodules present

$$\text{sensitivity} = \frac{\text{TPs}}{\text{TPs} + \text{FPs}}$$

Specificity: Number of TNs to total number of not detected nodules

$$\text{specificity} = \frac{\text{TNs}}{\text{FPs} + \text{TNs}}$$

6.3 Nodule Candidates Detection

We have evaluated the performance of parenchymal and juxtapleural nodule candidates detectors, i.e. only the detection part was tested.

Detectors work properly, each with sensitivity about 96%. The number of FPs is 12 FPs/slice, 6 from juxta-pleural, 6 from parenchymal detector. This justifies our decision to employ a further classification step to decrease the number of FPs. Results of nodule candidates detector testing are in Tables 6.1 and 6.2.

6.4 Classification Performance

For each examination both classifiers were learned. Detected and fitted nodules from other examinations were used for learning i.e. we used leave-one out method. Exams number 6 and 17 were treated apart, because the ground truth information was available in different format and would require manually redrawing of about 900 circles. After learning, detected and fitted nodule candidates were classified. The results from each examination separately are shown in Table 6.3. Confusion matrices for FLD based and multi-threshold classifiers are in Tables 6.4 and 6.5. Estimation of ROC for our algorithm is in Figure 6.1. Difference between statistic for juxtapleural and parenchymal nodules is shown in Table 6.8 for nodule candidates detection only, in Table 6.9 for multi-threshold classifier applied on detected nodule candidates and in Table 6.10 for FLD classifier applied on detected nodule candidates. Visualization of some results are in Figures 7.1–7.13. Table 6.6 shows comparison to other works.

Time consumption of one examination processing is about six hours. If nodule candidates are not fitted and classified, time to process examination decreases to one and half hour.

Dataset	Number of slices	Ground Truth		Sensitivity [%]		FPs/slice	
		Par.	Jux.	Par.	Jux.	Par.	Jux.
1	295	1	0	100.0		6.5	5.6
2	201	16	8	93.8	100.0	7.0	5.8
3	305	1	0	100.0		6.3	5.8
4	268	0	8		75.0	6.9	6.6
5	276	0	2		100.0	6.3	6.4
6	306	62	9	93.5	100.0	7.8	5.4
7	245	1	1	100.0	100.0	6.0	5.4
8	306	26	0	100.0		6.4	5.1
9	246	1	2	100.0	100.0	4.4	5.7
10	337	0	2		100.0	6.7	6.1
11	251	0	1		100.0	7.0	6.2
12	243	1	1	100.0	100.0	6.1	5.9
13	266	11	24	100.0	100.0	6.0	5.2
14	264	1	7	0.0	85.7	4.3	5.9
15	265	4	4	100.0	100.0	6.2	5.7
16	276	1	0	100.0		4.8	5.0
17	271	21	5	100.0	100.0	7.6	5.4
18	241	1	0	100.0		6.9	5.2
Total	4862	148	74	95.9	95.9	6.3	5.7

Table 6.1: Experimental results of nodule candidate detection

TP= 213	FN= 9
FP= 58359	TN= —

Table 6.2: Confusion matrix of nodule candidate detection

Dataset	Number of slices	Ground Truth		Sensitivity [%]				Specificity [%]				FPs/slice			
				FLD		Threshold		FLD		Threshold		FLD		Threshold	
		Par.	Jux.	Par.	Jux.	Par.	Jux.	Par.	Jux.	Par.	Jux.	Par.	Jux.	Par.	Jux.
1	295	1	0	100.0		100.0		82.5	77.8	26.7	21.0	1.1	1.2	4.8	4.4
2	201	16	8	93.8	75.0	87.5	87.5	74.8	66.0	18.9	18.6	1.9	2.0	5.7	4.7
3	305	1	0	100.0		100.0		85.8	75.8	26.8	24.6	0.9	1.4	4.6	4.4
4	268	0	8		50.0		62.5	81.3	78.2	31.5	26.8	1.3	1.4	4.7	4.8
5	276	0	2		100.0		100.0	80.4	78.0	23.0	30.8	1.2	1.4	4.9	4.5
6	306	62	9	75.8	22.2	88.7	88.9	85.9	69.8	33.2	25.6	1.3	1.6	5.2	4.0
7	245	1	1	100.0	100.0	100.0	100.0	84.1	77.2	21.0	22.4	1.0	1.2	4.8	4.2
8	306	26	0	73.1		96.2		83.0	61.2	30.0	26.4	1.2	2.0	4.5	3.8
9	246	1	2	0.0	50.0	100.0	100.0	70.7	75.6	19.4	26.4	1.3	1.4	3.5	4.2
10	337	0	2		0.0		50.0	82.4	75.7	30.7	22.1	1.2	1.5	4.7	4.7
11	251	0	1		100.0		100.0	82.2	76.4	20.4	21.5	1.2	1.5	5.5	4.9
12	243	1	1	100.0	100.0	100.0	100.0	83.7	79.7	18.6	20.3	1.0	1.2	5.0	4.7
13	266	11	24	90.9	87.5	100.0	95.8	80.9	78.0	18.5	22.8	1.2	1.3	4.9	4.0
14	264	1	7	100.0	100.0	100.0	85.7	72.7	73.5	23.6	36.8	1.2	1.6	3.3	3.7
15	265	4	4	50.0	75.0	75.0	100.0	85.0	78.4	30.0	27.6	0.9	1.2	4.3	4.1
16	276	1	0	100.0		100.0		80.6	76.5	22.0	27.7	0.9	1.2	3.8	3.6
17	271	21	5	76.2	0.0	90.5	60.0	84.5	74.1	22.6	26.0	1.3	1.4	5.8	4.0
18	241	1	0	100.0		100.0		82.9	78.7	27.0	20.7	1.2	1.1	5.1	4.2
Total	4862	148	74	78.4	66.2	91.2	86.5	81.5	75.0	25.3	25.0	1.2	1.4	4.7	4.3
Total		222		74.3		89.6		78.2		25.2		2.6		9.0	

Table 6.3: Experimental results of nodule candidates classification

TP= 165	FN= 57
FP= 12704	TN= 45655

Table 6.4: Confusion matrix of FLD classifier.

TP= 199	FN= 23
FP= 43652	TN= 17707

Table 6.5: Confusion matrix of multi-threshold classifier.

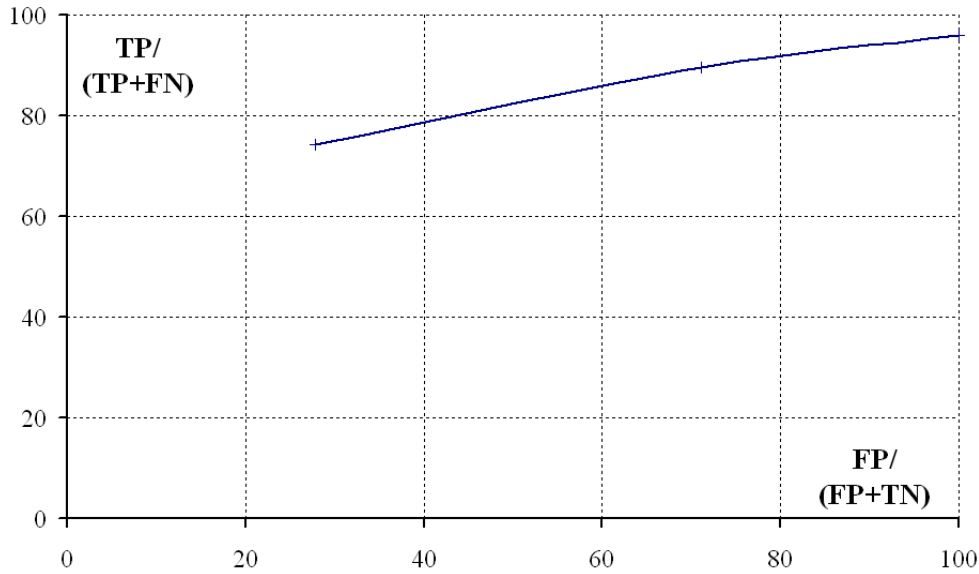


Figure 6.1: Estimation of ROC for our algorithm.

	Sensitivity [%]	FPs/slice	Testing data
Zhang [10]	85.6	0.04	real nodules >2mm
Zhao [5]	84.2	5	nodule model 2—7mm
Armato [40]	71	0.5	real nodules
Our detectors	95	12	real nodules >1.5mm
Our thr. class.	89.6	9	real nodules >1.5mm
Our FLD class.	74.3	2.6	real nodules >1.5mm

Table 6.6: Comparison of statistics among several works.

	Sensitivity [%]	Specificity [%]	FP/slice
Detection	95.9	—	12.0
FLD class.	74.3	78.2	2.6
Thr. class.	89.6	25.2	9.0

Table 6.7: Experimental results of algorithm

	Sensitivity [%]	Specificity [%]	FP/slice
Juxta-pleural n.	95.9	—	5.7
Parenchymal n.	95.9	—	6.3

Table 6.8: Difference between detection of juxta-pleural and parenchymal nodule candidates.

	Sensitivity [%]	Specificity [%]	FP/slice
Juxta-pleural n.	86.5	25.0	4.3
Parenchymal n.	91.2	25.3	7.7

Table 6.9: Difference between classification of juxta-pleural and parenchymal nodule candidates by multi-threshold classifier.

	Sensitivity [%]	Specificity [%]	FP/slice
Juxta-pleural n.	66.2	75.0	1.4
Parenchymal n.	78.4	81.5	1.2

Table 6.10: Difference between classification of juxta-pleural and parenchymal nodule candidates by FLD based classifier.

7 Conclusions

To find reliable method for nodule detection is an important problem in medicine. By starting a screening program based on this method, survival rate should be improved because of early detection of lung cancer.

We have developed an automatic method for the nodule detection. We are using two steps for ROI detection and lowering number of FPs among the detected nodule candidates. Also some volumetric information about nodules can be obtained from our method. The method was validated on data with 222 real nodules.

Our system performance can be adjusted between total sensitivity 95.9% with 12FPs/slice (when no classifier used) and total sensitivity 74.3% (when FLD based classifier applied). See Table 6.7.

There are some nodule-like object in testing data detected by algorithm and not included in ground truth information. These are probably nodules missed by human. (see Figure 7.10)

Our system was developed with Faculty Hospital, Motol, Prague and in future should be used there.

7.1 Future Work

Acceleration. System can be hardly accelerated by new fitting algorithm.

New descriptors. Classification can be improved by new shape descriptors of nodule.

Sensitivity control. User can choose not only from three types of classification (none, FLD, multi-threshold), but set working point anywhere on ROC.

Image Appendix

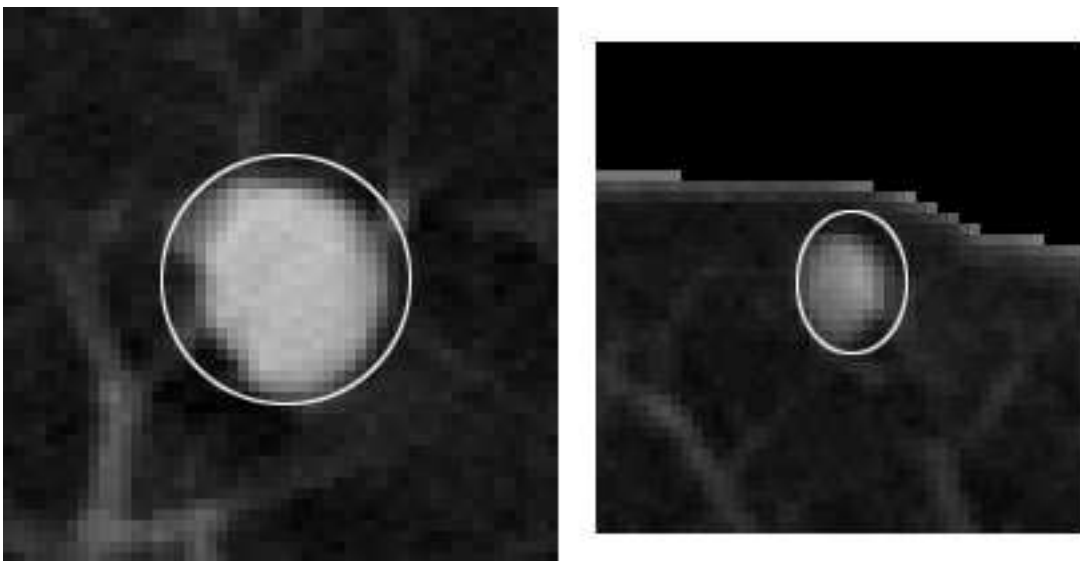


Figure 7.1: Examples of ellipsoids fitted on the nodule.



Figure 7.2: Input slice (left) and only non-pleural nodule candidates detected (right) white FPs, red TPs.



Figure 7.3: Nodules from Figure 7.2 after classifying by FLD based classifier (left) and multi-threshold classifier (right).



Figure 7.4: Input slice (left) and only non-pleural nodule candidates detected (right) white FPs, red TP.

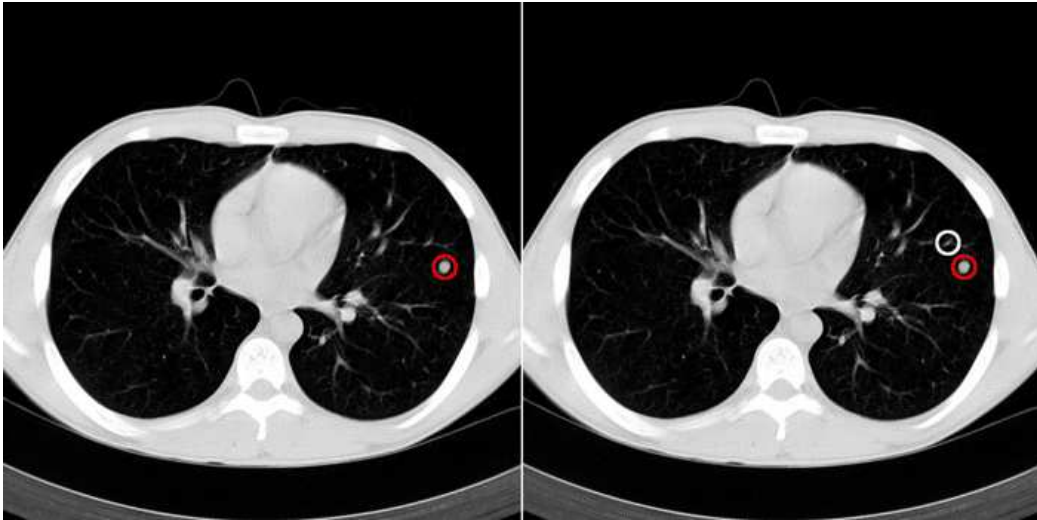


Figure 7.5: Nodules from Figure 7.4 after classifying by FLD based classifier (left) and multi-threshold classifier (right).

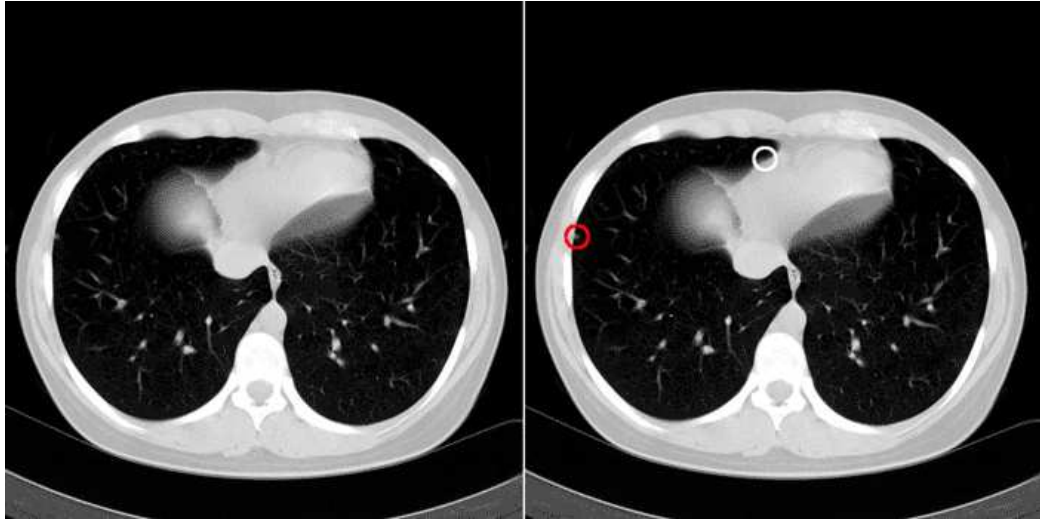


Figure 7.6: Input slice (left) and only non-pleural nodule candidates detected (right) white FPs, red TP.

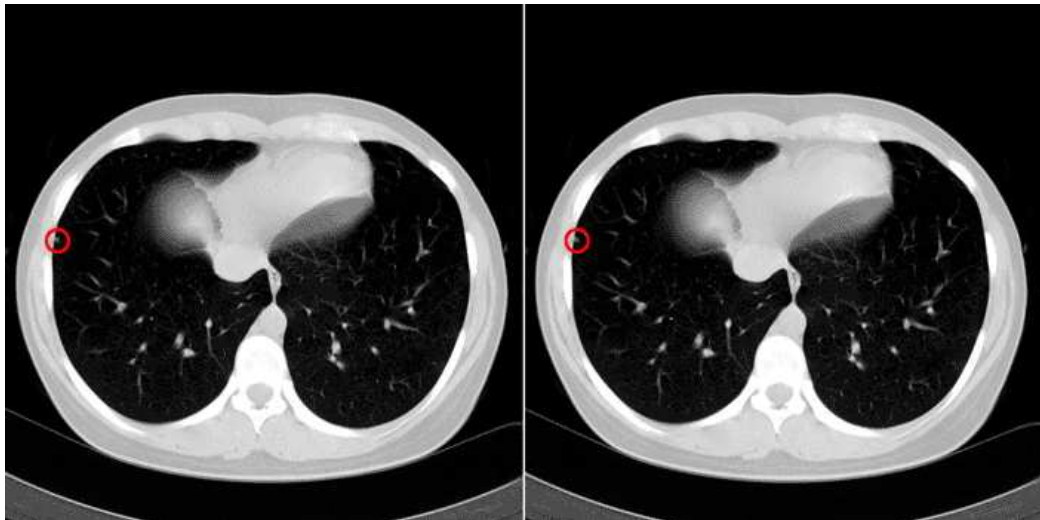


Figure 7.7: Nodule from Figure 7.6 after classifying by FLD based classifier (left) and multi-threshold classifier (right).

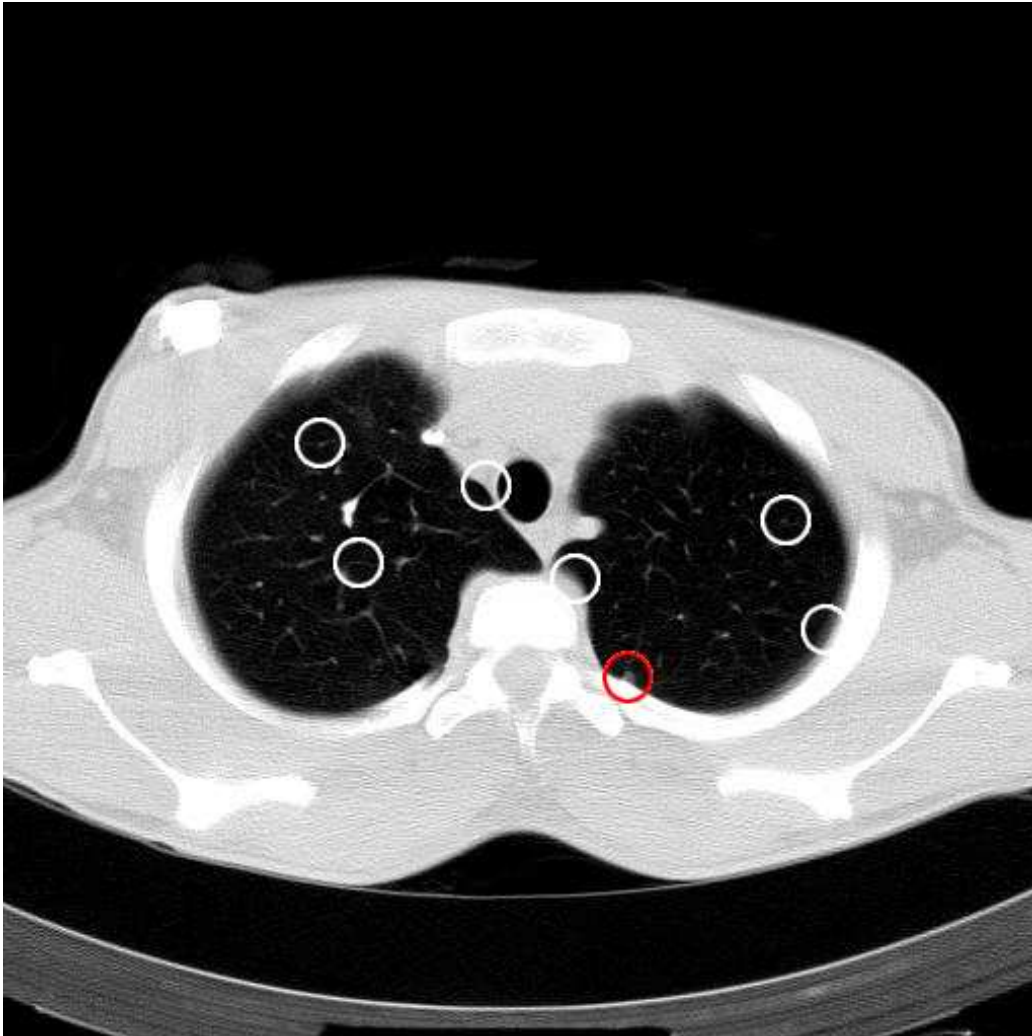


Figure 7.8: Example of output image. Multi-threshold classifier used for classification. Color added manually. TP (red), FPs (white)

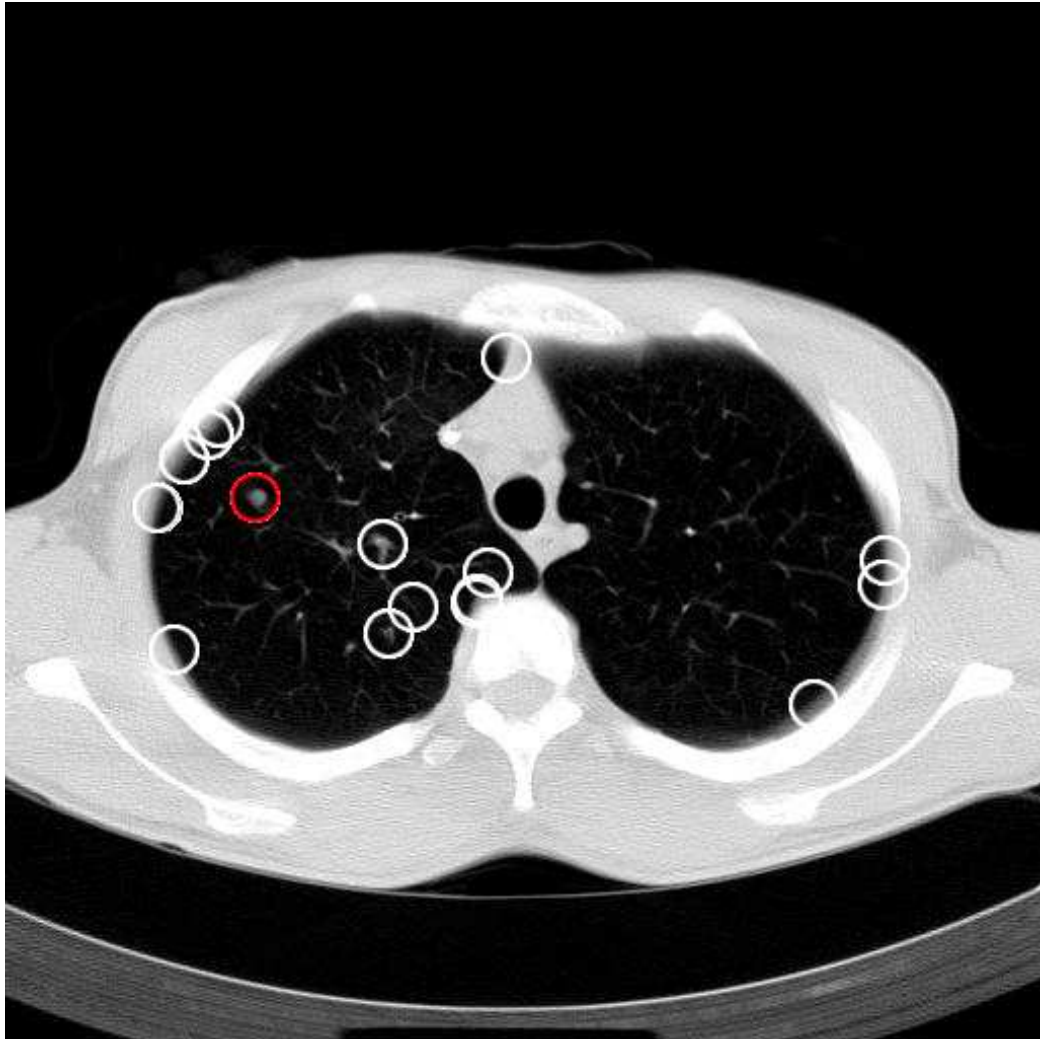


Figure 7.9: Example of output image. Multi-threshold classifier used for classification. Color added manually. TP (red), FPs (white)

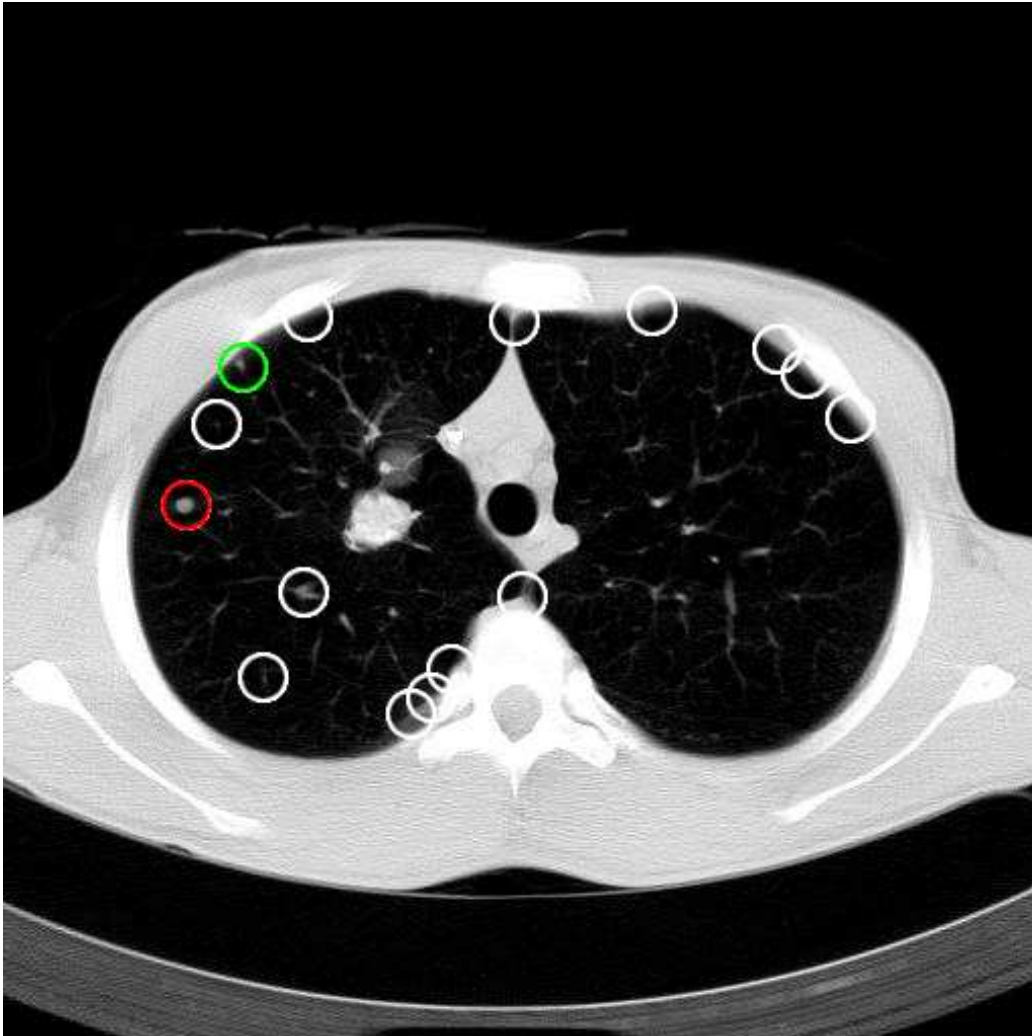


Figure 7.10: Example of output image. Multi-threshold classifier used for classification. Colors added manually. Object marked by green color is probably juxta-pleural nodule missed by human and detected by algorithm. TP (red), FPs (white)

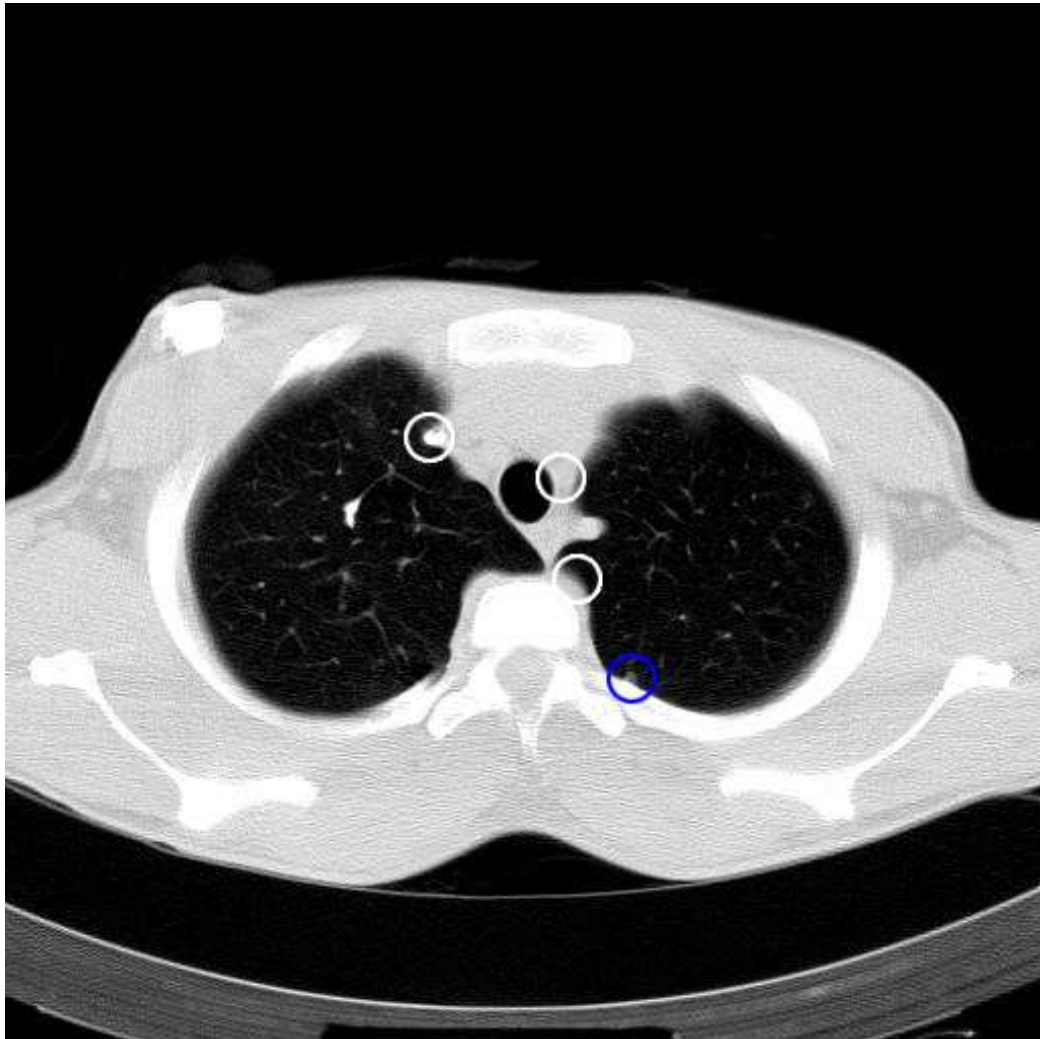


Figure 7.11: Example of output image. FLD based classifier used for classification. Colors and FN added manually. TP (red), FPs (white), FN (blue)

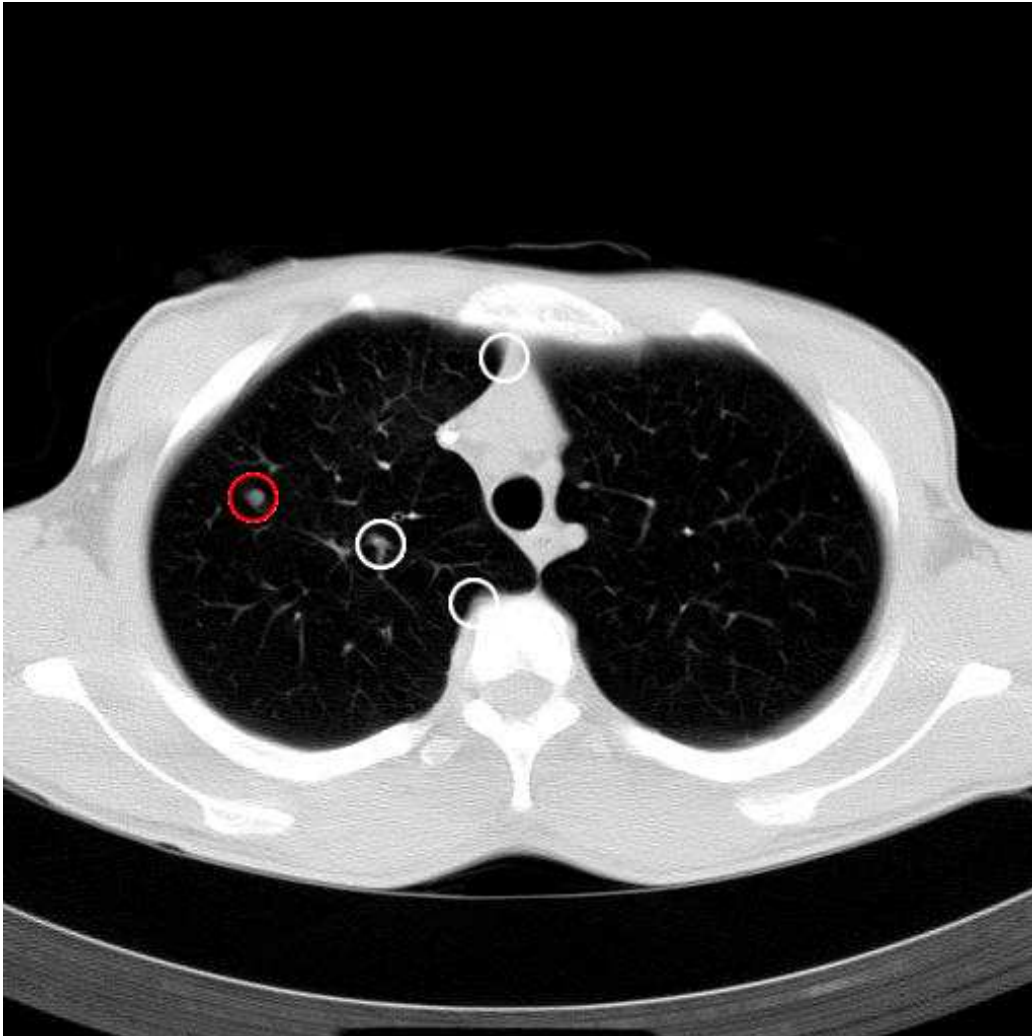


Figure 7.12: Example of output image. FLD based classifier used for classification. Colors added manually. TP (red), FPs (white)

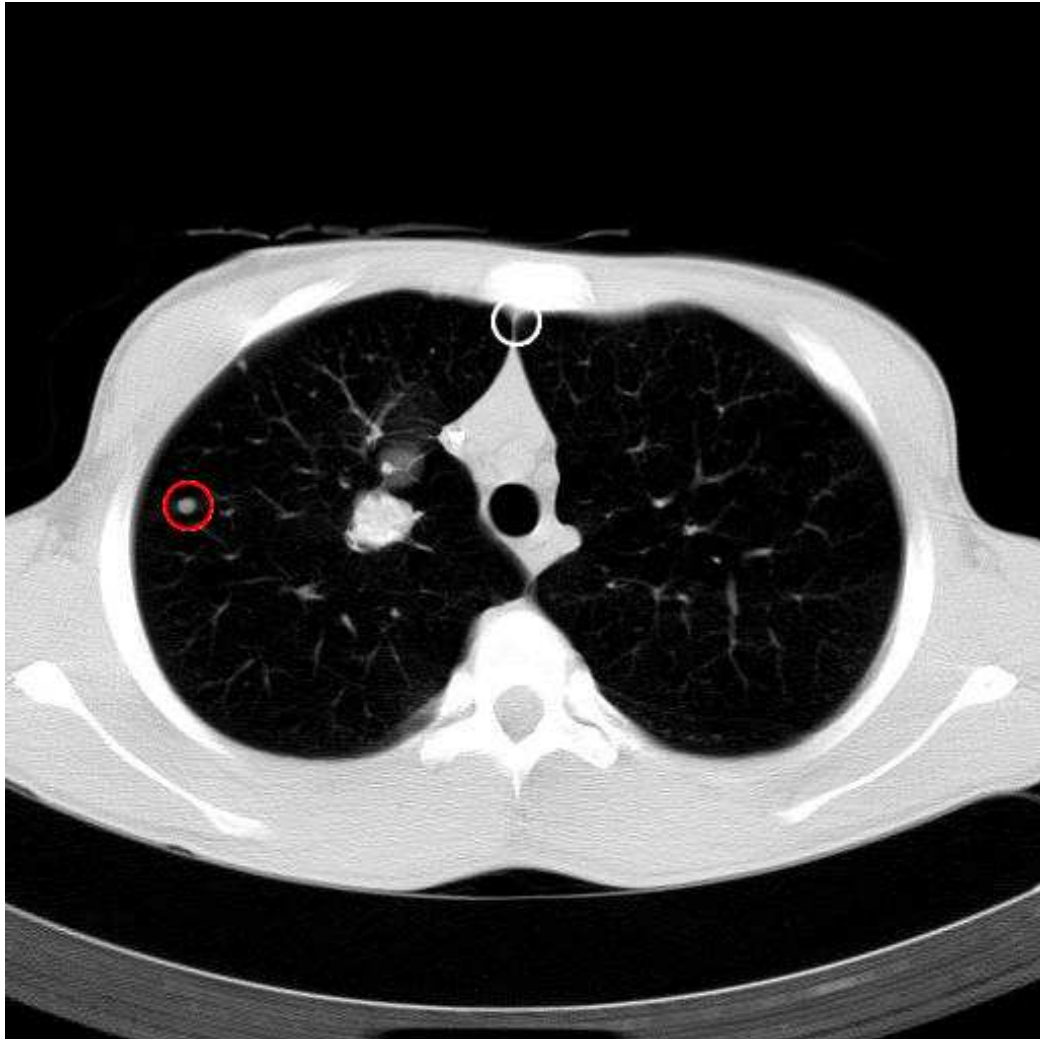


Figure 7.13: Example of output image. FLD based classifier used for classification. Colors added manually. TP (red), FPs (white)

Bibliography

- [1] D. P. Naidich, H. Rusinek, G. McGuinness, B. Leitman, D. I. McCauley, C. I. Henschke. *Variables affecting pulmonary nodule detection with computed tomography: evaluation with three-dimensional computer simulation*. J. Thorac Imaging no. 8.
- [2] J. W. Gurney: *Missed lung cancer at CT. imaging findings in nine patients* Radiology no. 199, 1996.
- [3] J. A. Buckley, W. W. Scott, S. S. Siegelman, J. E. Kuhlman, B. A. Urban, D. A. Bluemke, E. K. fishman *Pulmonary nodules: Effect of increased data sampling on detection with spiral CT and confidence in diagnosis*. Radiology no. 196, 1995.
- [4] S. E. Seltzer, P. F. Judy, D. F. Adams, F. L. Jacobson, P. Stark, R. Kikinis, R. G. Swensson, S. Hooton, B. Head, U. Feldman. *Spiral CT of the chest: comparison of cine and film-based viewing*. Radiology no. 197, 1995.
- [5] B. Zhao, G. Gamsu, M. S. Ginsberg, L. Jiang, L. H. Schwarz. *Automatic detection of small lung nodules on CT utilizing a local density maximum algorithm*. J. of applied clinical medical physics, vol. 4, no. 3, summer 2003.
- [6] B. van Ginneken, T. H. Romeny, M. A. Viergever. *Computer-Aided Diagnosis in Chest Radiography: A Survey*. IEEE Transactions on medical imaging, vol. 20, no. 12, 2001.
- [7] T. Lindeberg. *Feature Detection with Automatic Scale Selection*. J. of Computer Vision, vol. 30, no. 2, 1998.
- [8] R. O. Duda, P. E. Hart, D. G. Stork. *Pattern Classification*. John Wiley & Sons, 2nd. edition, 2001. Chapter 3
- [9] M. Sonka, V. Hlavac, R. Boyle. *Image Processing, Analysis, and Machine Vision*. PWS Publishing, 2nd. edition, 1998. ISBN 0-534-95393-X

- [10] X. Zhang, G. McLennan, E. A. Hoffman³, M. Sonka. *Automated detection of small-size pulmonary nodules based on helical CT images*. Springer Berlin/Heidelberg, 2005. ISSN 0302-9743
- [11] American Cancer Society. *ACS cancer facts and figures 2002*. American Cancer Society, Atlanta, GA, 2003.
- [12] L. Ries et al. *SEER Cancer Statistics Review 1973–1996*. National Cancer Institution, Bethesda, MD, 1999.
- [13] K. Okada. *Robust Anisotropic Gaussian Fitting for Volumetric Characterization of Pulmonary Nodules in Multislice CT*. IEEE Transaction on Medical Imaging, vol. 24, no.3. march 2005.
- [14] S. E. de Almeida e Mota. *Detection of Pulmonary Nodules Based on a Template-Marching Technique*. FEUP—Oporto University—Faculty of Engineering, 2003, available at <http://www.fe.up.pt/~ee98171/apsi/>
- [15] W. Lampeter, J. Wandtke. *Computerized Search of Chest Radiographs for Nodules*. Invest. Radiol., vol. 21, 1986, pp.384–390.
- [16] H. Yoshimura, M. Giger, K. Doi, H. MacMahon, S. Monther. *Computerized Scheme for the Detection of Pulmonary Nodules: A Nonlinear Filtering Technique*. Invest. Radiol., vol. 27, 1992, pp.124–127.
- [17] H. Yoshida, X. XU, K. Doi, M. Giger. *Computer-Aided Diagnosis (CAD) Scheme for Detecting Pulmonary Nodules Using Wavelet transforms*. Proc. SPIE, vol. 2434, 1995, pp. 621–626.
- [18] M. Geiger, K. Doi, H. MacMahon, C. Metz, F. F. Yin. *Pulmonary Nodules: Computer-Aided Detection in Digital Chest Images*. Radiographics, vol. 10, 1990, pp. 41–54
- [19] X. xu, H. MacMahon, M. Giger, K. Doi. *Adaptive Feature Analysis of False Positives for Computerized Detection of Lung Nodules in Digital Chest Radiographs*. Proc. SPIE, vol. 3034, 1997, pp. 428–436.
- [20] Q. Li, S. Katsuragawa, R. Engelmann, S. Armoto, H. MacMahon, K. Doi. *Development of a Multiple-Templates Matching Technique for Removal of False Positives in Computer-Aided Diagnostic Scheme*. Proc. SPIE, vol. 4322, 2001, pp. 1763–1770.
- [21] J. P. Ko, M. Betke. *Chest CT: Automated Nodule Detection and Assessment of Change Over Time—Preliminary experience*. Radiology 218, 2001, pp. 267–273.

- [22] M. L. Giger, K. T. Bae, H. MacMahon. *Computerized detection of pulmonary nodules in computed tomography images*. Invest. Radiol., vol. 29, 1994, pp. 459–465.
- [23] S. G. Armato, M. L. Giger, H. MacMahon. *Automated detection of lung nodules in CT scans: Preliminary results*. Med. Phys., vol. 28, 2001, pp. 1552–1561.
- [24] M. Fiebich, C. Wietholt, B. C. Renger, S. Armato, K. Hoffmann, D. Wormanns, S. Diederich. *Automatic detection of pulmonary nodules in low-dose screening thoracic CT examinations*. Proc. SPIE, vol. 3661, 1999, pp. 1434–1439.
- [25] L. Fan, C. L. Novak, J. Qian, G. Kohl, D. P. Naidich. *Automatic detection of lung nodules from multi-slice low-dose CT images*. Proc. SPIE, vol. 4322, 2001, pp. 1828–1835.
- [26] H. Satoh, Y. Ukai, N. Niki, K. Eguchi, K. Mori, H. Ohmatsu, R. Kakinuma, M. Kaneko, N. Moriyama. *Computer aided diagnosis system for lung cancer based on retrospective helical CT images* Proc. SPIE, vol. 3661, 1999, pp. 1324–1335.
- [27] T. Okumura, T. Miwa, J. Kako, S. Yamamoto, M. Matsumoto, Y. Tatenno, T. Linuma, T. Matsumoto. *Image processing for computer-aided diagnosis of lung cancer screening system by CT (LSCT)*. Proc. SPIE, vol. 3338, 1998, pp. 1314–1322.
- [28] Y. Lee, T. Hara, H. Fujita, S. Itoh, T. Ishigaki. *Automated detection of pulmonary nodules in helical CT images based on an improved template matching technique*. IEEE Transaction on Medical Imaging, vol.20, 2001, pp. 595–604.
- [29] S. Lou, C. Chang, K. Lin, T. Chen. *Object-Based Deformation Technique for 3-D CT Lung Nodule Detection*. Proc. SPIE, vol. 3661, 1999, pp. 1544–1552.
- [30] M. S. Brown, M. F. McNitt-Gray, J. G. Goldin, R. D. Suh, J. W. Sayre, D. R. Aberle. *Patient-specific models for lung nodule detection and surveillance in CT images*. IEEE Transaction on Medical Imaging, vol.20, 2001, pp. 1242–1250.
- [31] H. Taguchi, Y. Kawata, N. Niki, H. Satoh, H. Ohmatsu, R. Kakinuma, K. Eguchi, M. Kaneko, N. Moriyama. *Lung cancer detection based on*

- helical CT images using curved surface morphology analysis*. Proc. SPIE, vol. 3661, 1999, pp. 1307–1314.
- [32] P. Croisille, M. Souto, M. Cova, S. Wood, Y. Afework, J. Kuhlman, E. Zerhouni. *Pulmonary nodules: improved detection with vascular segmentation and extraction with spiral CT*. Radiology, vol. 197, 1995, pp. 397–401.
- [33] Siemens AG, Medical Solutions. *Excellence in CT: SOMATOM Definition*. Siemens AG, November 2006, available at www.siemens.com/medical.
- [34] V. Franc, V. Hlavac. *Statistical Pattern Recognition Toolbox for Matlab, User's guide*. June 24, 2004, available at <ftp://cmp.felk.cvut.cz/pub/cmp/articles/Franc-TR-2004-08.pdf>
- [35] Deans, R. Stanley. *The Radon Transform and Some of Its Applications*. John Wiley & Sons, 1983.
- [36] The Pulmonology Channel. *Solitary Pulmonary Nodule: Overview*. [online] [cit. 20.12.2006], available at <http://www.pulmonologychannel.com/spn/>
- [37] J. Shiraishi, S. Katsuragawa, J. Ikezoe, T. Kobayashi, K. Komatsu, M. Matsui, H. Fujita, Y. Kodera, K. Doi. *Development of a digital image database for chest radiographs with and without a lung nodule: Receiver operating characteristic analysis of radiologists' detection of pulmonary nodule*. Amer. J. Roentgenol., vol. 174, 2000, pp.71–74. Database available at http://www.jsrt.or.jp/cdrom_nodules.html
- [38] M. McNitt-Gray, S. Armato, L. Clarke, G. McLennan, Ch. Meyer, D. Yankelevitz. *The Lung Imaging Database Consortium: Creating a Resource for the Image Processing Research Community*. Cancer Imaging program, available at <http://imaging.cancer.gov/reportsandpublications/reportsandpresentations/firstdataset>
- [39] B. Sümenen *Blob detector*. [online] [cit. 12.5.2006] available at <http://barissumenen.com/myblog/index.php?id=3>
- [40] S. G. Armato, M. B. Altman, P. J. La Rivière. *Automated detection of lung nodules in CT scans: Effect of image reconstruction algorithm*. Medical Physics, vol. 30, no. 3, March 2003.

- [41] J. Beutel, H. L. Kandel, R. L. Van Mettel. *Handbook of Medical Imaging, Volume 2. Medical Image Processing and Analysis*. SPIE Press, 2000, ISBN 0-8194-3622-4.